JCI The Journal of Clinical Investigation

HPV16 drives cancer immune escape via NLRX1-mediated degradation of STING

Xiaobo Luo, … , Qianming Chen, Yu L. Lei

J Clin Invest. 2019. https://doi.org/10.1172/JCI129497.

Research In-Press Preview Immunology Oncology

Graphical abstract

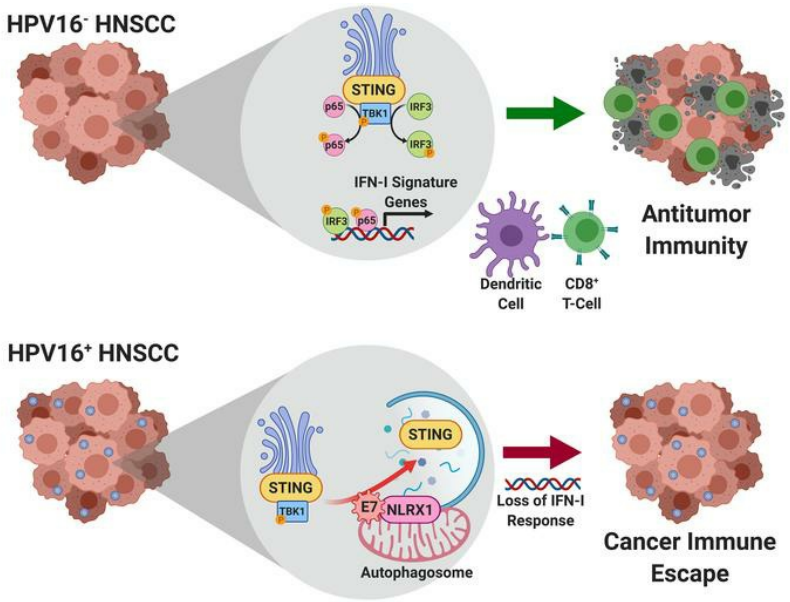

Title: HPV16 drives cancer immune escape via NLRX1-mediated degradation of STING

Authors Xiaobo Luo[1,2], Christopher R. Donnelly[1,3], Wang Gong[1,2], Blake R. Heath[1,4], Yuning Hao[5], Lorenza A. Donnelly[1], Toktam Moghbeli[1], Yee Sun Tan[1,6], Xin Lin[1], Emily Bellile[6], Benjamin A. Kansy[7], Thomas E. Carey[6,8], J. Chad Brenner[6,8], Lei Cheng[2], Peter J. Polverini[1,3,6,9], Meredith A. Morgan[6,10], Haitao Wen[11], Mark E. Prince[6,8], Robert L. Ferris[12], Yuying Xie[5], Simon Young[13], Gregory T. Wolf[6,8], Qianming Chen[2,*], Yu L. Lei[1,3,4,6,8,*]

Affiliations

[1]Department of Periodontics and Oral Medicine, the University of Michigan School of Dentistry, Ann Arbor, Michigan, USA.

[2]State Key Laboratory of Oral Diseases, National Clinical Research Center for Oral Diseases, West China School of Stomatology, Sichuan University, Chengdu, Sichuan, China.

[3]Oral Health Sciences PhD Program, the University of Michigan School of Dentistry, Ann Arbor, Michigan, USA.

[4]Graduate Program in Immunology, University of Michigan Medical School, Ann Arbor, Michigan, USA.

[5]Department of Computational Mathematics, Science, and Engineering, Michigan State University, East Lansing, Michigan, USA.

[6]University of Michigan Rogel Cancer Center, Ann Arbor, Michigan, USA.

[7]Department of Otolaryngology, University Hospital Essen, Essen, North Rhine-Westphalia, Germany.

[8]Department of Otolaryngology – Head and Neck Surgery, the University of Michigan Health System, Ann Arbor, Michigan, USA.

[9]Department of Pathology, the University of Michigan Health System, Ann Arbor, Michigan, USA.

[10]Department of Radiation Oncology, the University of Michigan Health System, Ann Arbor, Michigan, USA.

[11]Department of Microbial Infection and Immunity, Ohio State University College of Medicine, the Ohio State University Comprehensive Cancer Center, Columbus, Ohio, USA.

[12]Department of Otolaryngology, Hillman Cancer Center, University of Pittsburgh School of Medicine, Pittsburgh, Pennsylvania, USA.

[13]Department of Oral & Maxillofacial Surgery, University of Texas Health Science Center at Houston, Houston, Texas, USA.

*Corresponding authors

Conflict of Interest: The authors have declared that no conflict of interest exists.

Keywords Head and Neck Cancer, NLRX1, type I interferon, HPV, STING

Financial Support This work is supported by NIH grants R01 DE026728, R00 DE024173, R03 DE027399, U01 DE029255, F31 DE028740, T32 AI007413, Rogel Cancer Center research committee grant, National Natural Science Foundation of China grants 81520108009, 81621062, 81730030, and the 111 MOE project of China. This study is supported by a Cancer Moonshot cooperative agreement, which requires an open access option upon acceptance by the journal.

Correspondence should be addressed to

Yu L. Lei, DDS, PhD

Address: 1600 Huron Parkway 2355, Ann Arbor, MI 48109

Phone: 734-615-6967

FAX: 734-763-5503

Email: leiyuleo@umich.edu

Qianming Chen, DDS, PhD

Address: Renmin Nan Street Section 3 #14, Chengdu, Sichuan 610041, China.

Phone : +86-28-85509709

Email: qmchen@scu.edu.cn

Text Word Count: 10,871. Total Number of Figures: 10. Total Number of Tables: 1

Total Number of Supplemental Figures: 9. Total Number of Supplemental Tables: 2

Abstract:

The incidence of human papillomavirus $(HPV)^+$ head and neck squamous cell carcinoma (HNSCC) has surpassed that of cervical cancer and is projected to increase rapidly until 2060. The co-evolution of HPV with transforming epithelial cells leads to the shutdown of host immune detection. Targeting proximal viral nucleic acid-sensing machinery is an evolutionarily conserved strategy among viruses to enable immune evasion. However, E7 from the dominant HPV subtype-16 in HNSCC shares low homology with HPV18 E7, which was shown to inhibit the STING-DNA-sensing pathway. The mechanisms by which HPV16 suppresses STING remain unknown. Recently, we characterized the role of the STING-type-I interferon (IFN-I) pathway in maintaining immunogenicity of HNSCC in mouse models. Here we extended those findings into clinical domain utilizing tissue microarrays and machine-learning-enhanced profiling of STING signatures with immune subsets. We additionally showed that HPV16 E7 employs distinct mechanisms than HPV18 E7 to antagonize the STING pathway. We identified NLRX1 as a critical intermediary partner to facilitate HPV16 E7-potentiated STING turnover. The depletion of NLRX1 resulted in significantly improved IFN-I-dependent T-cell infiltration profiles and tumor control. Overall, we discovered a unique HPV16 viral strategy to thwart host innate immune detection that can be further exploited to restore cancer immunogenicity.

Introduction:

The co-evolution of oncogenic viruses with transforming epithelial cells encourages pathogens to develop unique mechanisms that enable immune evasion. The type-I interferon (IFN-I) system is an ancient and powerful host first-line anti-viral defense strategy, which is conserved from human to bony fish Osteichthyes (1). Thus, viruses have to encode proteins that can block the activation of IFN-I for their replication, intercellular transmission and/or genome integration. Conceptually, these strategies may directly target the enhanceosome components of IFN-I, such as p65 and IRF3, to directly inhibit IFN-I gene transcription (2, 3). Recently, another major class of viral proteins has surfaced, which alternatively target the more proximal nucleic acid-sensing protein complexes including the Stimulator of Interferon Genes (STING) complex (4). This strategy adds another layer of viral control of the host innate immune signaling.

Human papillomavirus (HPV)-associated cancers have become an endemic worldwide. HPV is associated with several cancer types including cervical, anal, penile, and head and neck squamous cell carcinomas (HNSCC). Strikingly, the incidence rate of HPV-associated HNSCC has surpassed that of cervical cancer and will continue to increase until at least 2060, even after adjusting for the use of HPV vaccines among women (5). Despite the presence of viral epitopes in HPV^+ HNSCC, these tumors exhibit less T-cell clonal expansion than HPV^- tumors (6). In a

two-year long-term follow-up of a randomized phase 3 trial (CheckMate 141), it shows that HNSCC patients can benefit from anti-PD-1 therapy regardless of the HPV status. Notably, the Hazard Ratios (HR) were almost identical between the HPV^- and HPV^+ groups, despite the generally more favorable response profiles to chemotherapy among patients with HPV^+ tumors (7, 8). Similarly, pembrolizumab resulted in little survival improvement over standard-of-care in patients with $p16^+$ tumors enrolled in another randomized phase 3 trial KEYNOTE-040 (HR=0.97; 95% Confidence Interval: 0.63-1.49) (9). Thus, immunotherapy-mediated survival improvement appears to be lower than expected for HPV^+ tumors (10), despite their dense immune infiltrates and association with viral epitopes. Not surprisingly, HPV could encode IFN-I-inhibiting proteins to dampen innate immune sensing. For example, the HPV18 E7 oncoprotein was shown to bind with STING and inhibit its function (11). However, HPV18 is rare in HNSCC and accounts for less than 3% of HPV^+ cases whereas over 90% of HPV^+ HNSCC cancers are instead linked to HPV16 (12). More importantly, the E7 proteins encoded by HPV16 and HPV18 share a low-degree of homology, suggesting potential functional divergence. How HPV16 inhibits the IFN-I systems remains unknown.

This presents a significant knowledge gap as the manipulation of the IFN-I system can yield potentially transformative immune-priming outcomes. The current conceptual framework surrounding anti-tumor immunity centers on the relationship between cancer mutational load

and the number of tumor neoantigen-targeted cytotoxic T lymphocytes (CTLs), it remains unexplained why most HNSCC are hypoimmunogenic despite the presence of high mutation burdens and the presentation of HPV-associated neoantigens (13). To explain this dichotomy, we recently demonstrated that HNSCC cells evade immune surveillance through suppression of the STING-IFN-I pathway, a key adaptive resistance mechanism that limits effector T-cell expansion (14). IFN-I is produced by both cancer cells and antigen-presenting cells (APCs). IFN-I and its downstream chemokines create a strongly T_H1/Tc1-skewed milieu to promote APC tumor-trafficking and cross-presentation to $CD8^+$ CTLs (15-17). A second messenger and the physiological agonist of STING, cGAMP, has been exploited in different tumor models to improve CTL expansion (18-23). To prevent the expanded CTLs from rapidly entering into an exhaustion state, at least three ongoing clinical trials are assessing a combination strategy of STING agonist plus immune checkpoint blockade (NCT02675439, NCT03172936, and NCT03010176). Due to the highly polar molecular property, which may prevent cGAMP entering cytoplasm effectively to maximally activate STING, we engineered unique nanoparticles and slow release delivery systems to improve the pharmacodynamics of STING agonists. These efforts improved the delivery of cGAMP in vivo and sensitized hypoimmunogenic HNSCC to immune checkpoint blockade (14, 24).

STING is ubiquitously expressed by epithelial cells and immune cells. Thus, an in-depth examination of the mechanisms underpinning HPV16-mediated cancer-specific suppression of STING could reveal novel cancer immune escape strategies and identify potential intervention points to prime cold epithelial malignancies for checkpoint inhibitors. In this study, we sought to comprehensively annotate the relationship between STING-IFN-I signatures and tumor-infiltrating lymphocytes (TIL) subsets in clinical HNSCC specimens and reveal the mechanisms by which HPV16 evades from STING-induced IFN-I activation.

Results:

Deconvolution of the immune landscape of human HNSCC

To better quantify the TIL subsets present within the tumor microenvironment (TME), we engineered a novel and robust machine learning tool, Fast and Robust Deconvolution of Tumor Infiltrating Lymphocyte from Expression Profiles (FARDEEP), which exhibits less susceptibility to data outliers that are universally present in whole tissue RNA-Seq data-sets (25). We quantitated TILs in 520 HNSCC specimens from the TCGA database, including 97 HPV^+ and 420 HPV^- tumors that involve oral cavity, oropharynx, and larynx. We found an extensive infiltration of regulatory T-cells (Treg), resting dendritic cells and M2-like macrophages in the TME. The infiltration of $CD8^+$ T-cells, γδ T-cells, activated memory T-cells (Tmem), M1-like macrophages and activated natural killer (NK)-cells, which are essential to launching a tumor-specific immunologic attack, is highly variable across the specimens (Figure 1A). To thoroughly characterize the relationship between STING signatures and TIL distribution, we performed a marginal correlation analysis. We noted a robust positive correlation of STING signatures including *STING*, *MX1*, *CXCL9*, *CXCL10*, *ISG15*, and *ISG54* with intratumoral infiltration of M1-like macrophages, γδ T-cells, Tmem, $CD8^+$ T-cells, and NK cells. STING signaling is inversely correlated with the presence of naïve $CD4^+$ T-cells, follicular helper T-cells, plasma cells, and

neutrophils (Figure 1B), the last of which were found to be a significant prognosticator for a poor outcome in a pan-cancer study (26).

STING is a favorable prognosticator of HNSCC

Next, we sought to establish the clinicopathologic correlation of STING expression in HNSCC. We examined the survival data available from the TCGA, and found that high *STING* expression levels are significantly associated with improved prognosis in younger patients (p=0.005) (Figure 1C). When the Kaplan-Meier analysis is extended to all patients (n=520), STING remains a trending positive prognosticator (p=0.06) (Figure 1D). STING is broadly expressed in tumor cells and a variety of cell types in the TME. RNA-Seq data cannot distinguish the contribution of STING levels from different sources and may not be entirely concordant with protein expression. Thus, we constructed a tissue microarray (TMA) using 297 previously non-treated HNSCC specimens, 3 tumor cores for each specimen with a total of 891 cores, representing tumors of the larynx, hypopharynx, oral cavity, oropharynx, and other sites. The median follow-up at the time of analysis was 60.1 months. STING staining in HNSCC parenchyma and TME were independently defined and quantitated using Aperio ImageScope as we described previously (14, 27). Upon removal of cores with insufficient tumor tissue, STING staining scores were available from 264 HNSCC specimens. This cohort contains 32%

HPV^+ and 60% HPV^- HNSCC, and the demographic details are summarized in Supplemental Table 1. In agreement with the in-silico analysis of TCGA patients, we found that higher STING IHC staining scores are significantly correlated with improved patient survival (Figure 1E; p=0.027). Univariable Cox regression analysis found that higher STING scores in HNSCC parenchyma (p=0.01) and in TME (p=0.04) are both positively correlated with improved patient survival. Then, we built a multivariate Cox regression model controlling age, stage, site, HPV, and smoking. We found that STING expression in the tumor parenchyma remains a favorable prognosticator (p=0.049) while the STING staining scores of the TME are no longer significant (p=0.12), suggesting the critical importance of STING protein levels in HNSCC cancer cells in overall patient outcome (Table 1).

As the average age of patients with HPV^+ tumors is younger, our observation that the expression levels of STING are inversely correlated with patient age (Supplemental Figure 1A) prompted us to investigate whether this is due to an HPV-STING interaction term. Indeed, we identified a significant interaction term between HPV and the protein expression levels of STING (p=0.046). We also assessed the HPV-mRNA levels of *STING* interaction term using the TCGA database. Interestingly, an interaction is not identified (the corresponding p-values for the population with an age less than 60 and all patients are 0.81 and 0.46, respectively), suggesting that HPV is more relevant to the post-translational regulation of STING expression. After

stratifying the tumors by HPV status, STING is strongly associated with patient survival in HPV^+ group but not in the HPV^- group using multivariate Cox models (Supplemental Figure 1B and Supplemental Table 2).

HPV16 E7 suppresses STING signaling in HNSCC cells

The clinical findings prompted us to further investigate the interaction between HPV and STING signaling. HPV likely evolves anti-IFN-I strategies to make the host cells more permissive to viral replication and integration. Indeed, HPV18 E7 was previously shown to interact with and inhibit STING (11). However, only 3% of HPV^+ HNSCCs are positive for HPV18, while more than 90% of HPV^+ HNSCC is positive for HPV16 (5, 28). More importantly, upon a sequence homology analysis between E7 proteins encoded by HPV16 and HPV18, we found only 40% of homology between the two E7 proteins (Supplemental Figure 2), suggestive of molecular and functional divergence. Notably, when we transfected the physiological STING agonist, cGAMP, into $HPV16^+$ 93VU147T and UMSCC47 cells, no IFN-I signaling induction was observed, in contrast to cGAMP-induced IFN-I signaling in HPV^- UMSCC49 cells (Supplemental Figure 3A-C). To determine the specific role of HPV16 E7 in the regulation of the STING-IFN-I pathway, we first examined whether enhanced expression of HPV16 E7 protein modulates IFN-I signaling in 93VU147T and UMSCC47, which contain low-to-intermediate genomic copy

numbers of HPV16 (29). Upon analysis of the expression of *IFNB1* and two essential downstream IFN-I target genes, *CXCL10* and *ISG54*, we found that HPV16 E7 potently suppresses STING-induced immune activation (Figure 2A-F). In agreement, HPV16 E7 similarly inhibits cytoplasmic poly(dA:dT)-induced IFN-I signaling (Supplemental Figure 4A-B). To minimize the potential contribution of endogenous HPV16 E7 in these cell lines, we repeated these experiments in an HPV$^-$ HNSCC cell line, FaDu. Consistent with our previous results, HPV16 E7 suppresses STING-mediated immune activation (Figure 2G-I). To confirm the findings with *IFNB1* transcripts, we performed ELISA to quantitate the protein levels of IFN-β in the supernatant. STING induces the production of IFN-β by 93VU147T, UMSCC47, and FaDu cells; HPV16 E7 largely abolished STING-mediated immune induction (Figure 2J-L).

HPV16 E7 suppresses STING through an interaction-independent mechanism

Given the low sequence homology between the HPV16 E7 and HPV18 E7 oncoproteins, we speculated that HPV16 E7 could suppress STING signaling through a distinct mechanism from HPV18 E7. To determine whether HPV16 E7 can directly associate with STING, like HPV18 E7, we performed a semi-endogenous co-immunoprecipitation (co-IP) in 93VU147T cells expressing HA-tagged STING. We were unable to detect an HPV16 E7-STING association even in the presence of STING overexpression. The expression of HPV16 E7 was confirmed in

the input samples (Figure 3A). A mitochondrial member of the NOD-like receptor (NLR) family, NLRX1, recently shown to directly bind STING (30), was used as a positive control for the quality of co-IP, with NLRX1-deficient cells serving as an additional control.

Since HPV16 E7 does not associate with STING, we hypothesize that HPV16 E7 may target STING by interfering with its turnover. Thus, we next investigated whether the levels of HPV16 E7 expression are inversely correlated with those of STING in HNSCC cells. To this end, we screened a panel of HNSCC cells which included four HPV^+ and two HPV^- cell lines. We found UMSCC47 to have a low level of expression of HPV16 E7, 93VU147T cells to have an intermediate level of HPV16 E7, and UDSCC2 and SCC90 to have the highest levels of endogenous HPV16 E7 (Figure 3B). These findings are concordant with previous reports of HPV16 genome copy numbers in these cell lines (29). Interestingly, we observed an inverse correlation between HPV16 E7 and STING protein levels, wherein high levels of HPV16 E7 were associated with decreased levels of STING protein (Figure 3B). To validate whether HPV16 E7 inhibits downstream STING signaling, we analyzed whether STING-dependent phosphorylation of TANK Binding Kinase 1 (TBK1) was altered by varying expression levels of HPV16 E7. We observed a significant decrease in STING levels in 93VU147T, UMSCC47, and FaDu cells (Figure 3C-E) following exogenous expression of HPV16 E7. Additionally, we

observed a decrease in phosphorylation of TBK1 (phospho-S172, normalized to total TBK1) with increased levels of HPV16 E7 (Figure 3C-E). These results substantiate HPV16 E7 as an important suppressor of STING and STING-dependent IFN-I responses.

HPV16 E7 promotes autophagy-dependent degradation of STING

To understand how HPV16 promotes the turnover of STING protein, we examined existing literature for STING regulation. Autophagy, as a central process maintaining cellular homeostasis, is also frequently employed to control overzealous inflammation (31). In fact, innate immune signaling complexes, including STING, are found to be cargos for autophagosomes (14, 32-36). Thus, we posited that HPV16 E7 induces STING degradation via an autophagy-dependent mechanism. To this end, we analyzed LC3-II, a marker of autophagy induction, in 93VU147T, UMSCC47, and FaDu cells. Consistently, we observed that the expression of HPV16 E7 leads to decreased levels of STING protein and a marked increase in LC3B-II (Figure 4A-C). Further, we repeated these experiments in the presence of Bafilomycin A1 (BafA1), a pharmacological inhibitor of autophagy. We observed that BafA1 could partially reverse the HPV16 E7-induced loss of STING protein in 93VU147T cells (Figure 4D), and that inhibition of autophagy completely abolishes HPV16 E7-mediated degradation of STING in UMSCC47 (Figure 4E) and FaDu (Figure 4F) cells. These results suggest that HPV16 E7

accelerates STING turnover through an autophagy-dependent mechanism. To confirm HPV16 E7-mediated regulation of STING is a post-translational event, we further assessed whether HPV16 E7 decreases the mRNA levels of *STING*. We found that HPV16 E7 only has a modest effect on the mRNA transcription of *STING* in the three cell lines (Supplemental Figure 5A).

Genetic deletion of HPV16 *E7* restores STING-mediated IFN-I induction

To substantiate these findings, we next generated HPV16 $E7^{-/-}$ 93VU147T and UMSCC47 cell lines using CRISPR-Cas9 lentiviruses containing a sgRNA targeting HPV16 *E7*. Immunoblotting confirmed the loss of E7 protein in both knockout cell lines (Figure 5A-B). Notably, loss of HPV16 E7 leads to reduced autophagy, a striking restoration of STING protein levels, and elevated levels of phospho-TBK1 in 93VU147T and UMSCC47 cells under basal and induced conditions (Figure 5A-B). We next performed qPCR to examine the expression of IFN-I signature genes in these cells. We observed a significant increase in both basal and cGAMP-stimulated upregulation of *IFNB1*, *MX1*, *ISG15*, and *ISG54* in HPV16 $E7^{-/-}$ HNSCC cells compared to $E7^{+/+}$ controls (Figure 5C-D). To validate the transcription profile findings at protein levels, we performed ELISA to detect secreted IFN-β in the supernatant. Transfection of cGAMP cannot induce the production of IFN-β in wild-type 93VU147T and UMSCC47 cells; and the production of IFN-β is restored upon deletion of *E7* (Figure 5E). Last but not least, to confirm

whether autophagy is reduced by removal of HPV16 E7, as a mechanism of stabilizing STING protein levels, control or HPV16 *E7*$^{-/-}$ UMSCC47 cells were transfected with pEGFP-LC3B and imaged by confocal microscopy 48 hours later. In agreement with LC3B immunoblotting, we observed a significant loss of LC3B-GFP^{+} puncta (Figure 5F) upon deletion of *E7*, supporting the notion that loss of HPV16 E7 leads to a corresponding decrease in autophagy.

HPV16 E7 specifically interacts with NLRX1

Our previous studies discovered an NLRX1-centered molecular complex that potentiates autophagosome formation (27, 33). To determine whether HPV16 E7 intersects with this pathway as a mechanism promoting STING turnover, we first performed endogenous co-immunoprecipitation experiments (Figure 6A-B). After pulling down endogenous HPV16 E7-interacting protein complexes from 93VU147T and SCC90 cell lysates, we identified a specific interaction with endogenous NLRX1. Three types of controls were included: (a) isotype control antibody was used for the mock pull-down; (b) starting lysates from the isotype control group and HPV16 E7 Ab group were identical; (c) protein specificity controls were also included. HPV16 E7 does not interact with three abundant proteins that are localized in mitochondria (VDAC), cytoplasm (p63), or endoplasmic reticulum (STING). As a previous study suggests that HPV18 E7 interacts with STING as a mechanism of inhibiting STING signaling (11), we sought

to determine whether HPV16 E7 engagement with NLRX1-mediated autophagic machinery is specific to HPV16. We transduced HPV$^-$ UMSCC49 cells with HPV18 E7, and indeed identified an interaction between HPV18 E7 and STING. However, HPV18 E7 does not interact with NLRX1 and other aforementioned control proteins under our stringent buffer conditions (Figure 6C). Thus, here we show HPV16 and HPV18 E7 proteins utilize distinct mechanism to inhibit STING-mediated immune activation. Next, we performed a confocal imaging colocalization study to further confirm the interaction between HPV16 E7 and NLRX1. We stained 93VU147T cells with MitoTracker, NLRX1, and HPV16 E7 (Figure 6D). As validation of the staining quality, we show that NLRX1 co-localizes with mitochondria, as we previously reported (37). Interestingly, HPV16 E7 colocalizes with NLRX1 and mitochondria, in agreement with our findings in Figure 6A-B.

NLRX1 inhibits STING-IFN-I signaling in HPV16$^+$ HNSCC cells

Despite the well-characterized core proteins involved in autophagosome membrane initiation and elongation, the regulatory mechanisms are complex and cell type-dependent. Recently, we identified NLRX1 as an important contributor to autophagy in HNSCC (27), functioning as a protein complex scaffold recruiting autophagy-promoting molecules including ATG12–ATG5 and BECN1 (27, 33). As HPV16 E7 specifically interacts with NLRX1, we sought

to determine whether HPV16 E7-induced STING turnover in cancer cells utilizes an NLRX1-dependent mechanism. We first examined the expression of NLRX1 in 4 HPV^+ HNSCC cells lines and found that 3 of 4 (93VU147T, UMSCC47, and SCC90) have high endogenous levels of NLRX1 protein (Figure 7A). To determine whether NLRX1 contributes to STING degradation in these HPV^+ cell lines, we generated stable NLRX1-deficient 93VU147T, UMSCC47, and SCC90 cell lines through shRNA transduction (shNLRX1, or EV, as a control). Due to low endogenous levels of STING in 93VU147T and SCC90 cells (Figure 3A), STING was expressed in EV and shNLRX1 cells 24 hours prior to harvest. Compared to EV controls, shNLRX1 cells show reduced autophagy and substantially increased protein levels of STING (Figure 7B-D). Consistently, a defect in NLRX1 results in a significant increase in the expression of IFN-I signature genes *IFNB1, ISG15, CXCL9,* and *CXCL10* (Figure 7E-F), an effect which was consistent across the HNSCC cell lines analyzed. As a control, we found NLRX1 does not affect the mRNA levels of *STING* (Supplemental Figure 5B), suggesting that NLRX1-mediated inhibition of STING signaling occurs at post-transcriptional levels. We also analyzed the phosphorylation of TBK1 and p65 to determine whether downstream STING signaling is restored in shNLRX1 93VU147T and SCC90 cells. In agreement, we observed increased ratios of pTBK1/TBK and p-p65/p65 in shNLRX1 93VU147T and SCC90 cells compared to EV controls (Figure 7G).

NLRX1 suppresses STING-mediated immune detection of E7-expressing tumors in vivo

Recently, we characterized a new HPV16 E6/E7-expressing HNSCC mouse model, MOC2-E6/E7, which is syngeneic to C57BL/6 (14, 24, 38). These tumors grow aggressively and are completely resistant to immune checkpoint blockade therapy (14, 39). To determine whether NLRX1 inhibits cancer immunogenicity by targeting the STING-IFN-I pathway, we generated stable NLRX1-deficient MOC2-E6/E7 cells using lentiviruses targeting *NLRX1* (or empty vector lentivirus as a control, EV). Wild-type and NLRX1-deficient tumor cells were transfected with a STING agonist poly(dA:dT). Then, we analyzed the expression levels of IFN-I signatures *Ifnb1*, *Mx1*, *Isg15*, and *Isg54* 16 hours post-induction (Figure 8A). In agreement with the results obtained in the human cell lines, we observed that NLRX1-deficient MOC2-E6/E7 cells exhibit significantly enhanced STING activation. To further support these results, we expressed murine STING in control and NLRX1-deficient MOC2-E6/E7 cells and confirmed that NLRX1 deficiency results in enhanced STING signaling, evidenced by increased phospho-TBK1 (Figure 8B).

Depletion of NLRX1 has minimal effect on the rates of cell proliferation (Figure 8C). However, NLRX1-deficient tumors exhibit a significant reduction in tumor burden in wild-type C57BL/6 hosts (Figure 8D; p=0.02), with 14 of 19 NLRX1-deficient tumors completely rejected. Whole tumors were homogenized and the qPCR analysis performed. We found that NLRX1-

deficient tumors show significantly elevated expression levels of the *Tnf*, *Il6*, and *Ifnb1,* key markers for STING-mediated downstream effector activation (Figure 8E) (40). Il10 was identified as a prominent immunosuppressive factor in MOC2-derived tumors (41), thus, we additionally assessed the transcription levels of Il10. We found that Il10 was trending decreased in the NLRX1-deficient tumors (p=0.08) (Supplemental Figure 6). Consistently, we examined the histology of control and NLRX1-deficient tumors, and found that more inflammatory infiltrates are present in the tumor-stroma interface in the NLRX1-deficient tumors than control specimens (Supplemental Figure 7A). We stained the specimens with anti-CD8 and noted an increase in CD8 immune cells in the TME of NLRX1-deficient tumors (Supplemental Figure 7B). To better characterize the immune infiltrates, TILs and immune cells from draining lymph nodes were purified from mice with EV- or shNLRX1-MOC2-E6/E7 tumors via a Ficoll-Paque gradient and analyzed by flow cytometry. We found that *NLRX1*-deficient tumors harbor significantly reduced $CD3^+CD4^+Tim3^+$ and $CD3^+CD8^+Tim3^+$ T-cells (Figure 8F), which are functionally exhausted in HNSCC specimen (42). NLRX1-deficient-tumor-bearing mice also show better CTL expansion in the draining lymph nodes (Figure 8G).

NLRX1-mediated inhibition of anti-tumor immunity is IFN-I-dependent

As autophagy has pleiotropic effects on a variety of pathways, we next sought to determine whether the shNLRX1-mediated tumor rejection we observed in vivo is indeed T-cell- and IFN-I-dependent. To this end, we first depleted $CD8^+$ T-cells using a monoclonal antibody; and depletion was confirmed using flow cytometry (Supplemental Figure 8). We found that depletion of $CD8^+$ T-cells largely rescued NLRX1 deficiency-mediated tumor rejection, although NLRX1-deficient tumors were slightly smaller, suggesting the involvement of other TIL subsets in addition to CTL (Figure 9A). No difference was observed for a panel of effector cell markers (Figure 9B). To more thoroughly test the phenotype dependence on adaptive immune response, we established EV- or shNLRX1-MOC2-E6/E7 tumors in B-cell- and T-cell- deficient *Rag1*$^{-/-}$ hosts. In contrast to the results in wild-type C57BL/6 hosts (Figure 8D), we observed no difference in tumor growth between control and NLRX1-deficient tumors (Figure 9C), as well as comparable levels of STING signature genes transcription from whole tumor homogenates (Figure 9D). Then, we repeated these experiments in *Ifnar1*$^{-/-}$ hosts, which contain a deletion of IFN-I receptor *Ifnar1* and show abolished IFN-I signaling. Similarly, we did not observe any differences in tumor volumes between EV- and shNLRX1-MOC2-E6/E7 tumors (Figure 9E), or in the transcription of Sting signature genes within the TME (Figure 9F).

In order to further characterize the relationship between NLRX1 and TIL distribution in HNSCC, we performed a correlation analysis of *NLRX1* expression and the quantity of different

TIL subsets in 78 HPV16$^+$ HNSCC specimens in the TCGA database. We found that the expression levels of *NLRX1* are significantly inversely correlated with the infiltration of CD8$^+$ T-cells (Spearman ρ=-0.42, p=0.00018), CD4$^+$ activated memory T-cells (Spearman ρ=-0.40, p=0.00039) and activated NK-cells (Spearman ρ=-0.27, p=0.022). A negative correlation with M1-like macrophages is also observed with a marginal p-value (Spearman ρ=-0.19, p=0.099) (Figure 10A). As proof of high-fidelity rendering of the immune infiltrate, we also performed correlation analysis between the expression levels of *STING* with different TIL subsets. We show that *STING* is significantly positively correlated with CD8$^+$ T-cells (Spearman ρ=0.24, p=0.040), CD4$^+$ memory T-cells (Spearman ρ=0.36, p=0.0016), γδ T-cells (Spearman ρ=0.41, p=0.00031), and M1-like macrophages (Spearman ρ=0.33, p=0.0039) (Figure 10B). Interestingly, these correlations are more prominent in HPV$^+$ HNSCC specimens compared to HPV$^-$ HNSCC specimens (Supplemental Figure 9), possibly owing to the role of NLRX1 in potentiating HPV16 E7-mediated STING suppression.

Discussion:

Throughout the course of co-evolution, the host has developed a battery of germline-encoded pattern recognition receptors (PRRs) to detect double-stranded DNA (dsDNA) viruses (43). Based on sequence homology and subcellular localization, the nuclei acids-sensing PRRs are classified into four major families: Toll-like receptors (TLR), NLRs (aka nucleotide-binding domain lots of leucine-rich repeats containing receptors), cGAS-STING cytoplasmic sensor and AIM2 inflammasome. An array of DNA viral proteins targets PRR members to establish persistent infections. Conceptually, three viral strategies are well established to disrupt host DNA-sensing pathways. (i) The DNA viruses may encode proteins to occupy host DNA sensors binding pocket to sequester viral genome from PRRs (44). (ii) Viral proteins may directly interact with innate immune signaling complex, such as the STING-TBK1 complex, to disrupt downstream signaling. HPV18 E7 utilizes this strategy to control the IFN-I system (11). (iii) DNA viral proteins may directly target distal IFN-I enhanceosome components to interfere with target gene transcription (2, 3).

This study reveals a novel dsDNA viral strategy to control the STING-IFN-I axis – protein destabilization. HPV16 and HPV18 are among the most common high-risk HPV subtypes that drive carcinogenesis. A plethora of studies on the biology of their oncoproteins leads to the revelation of the pathologically critical pRb interactome (45). Emerging evidence shows that

HPV oncoproteins also exhibit pleiotropic effects on the host innate immune system. The nonkeratinizing oropharyngeal squamous cell carcinomas are frequently HPV16-related and arise in the tonsillar crypts of palatine and lingual tonsils. This unique anatomic location is characterized by dense immune cell infiltration, which should constitute a potent immune defense. Thus, in order to establish an invasive front, the transforming basal layer cells need to develop a strategy to mitigate innate immune detection. Indeed, normal basal layer of squamous epithelium expresses STING (46), and the HPV16-induced turnover of STING likely dampens the "visibility" of the invasive fronts to the immune system. HPV16 E7 only has a low-degree of homology with its HPV18 counterpart and does not interact with the STING complex like HPV18 E7 does. Instead, HPV16 E7 hijacks a PRR member, NLRX1, to destabilize STING. The unique presence of viral proteins in HPV^+ tumors triggered enthusiasm for the development of therapeutic vaccines which enhance HPV protein-specific antitumor immunity (47). The viral epitopes were considered to be highly immunogenic. However, the clinical response of HPV^+ HNSCC to checkpoint immunotherapy is surprisingly low (8). In fact, HPV^+ HNSCC contains less CTL clonal expansion and exhibits lower levels of antigen-presenting machinery than HPV^- tumors (6). Hence, the findings from this study pinpoint a previously unknown strategy that HPV16 utilizes to inhibit the host processing of viral neoepitopes.

Harnessing the checkpoints for IFN-I induction could yield significant immune-priming benefits. Our recent unbiased screen using HNSCC cell-effector immune cell co-culture identified the IFN-I pathway as a central signal that maintains HNSCC sensitivity to immune killing (14). IFN-I downstream cytokines and chemokines improve APC and effector trafficking to the tumor mass and maintain a TME that favors APC maturation and cross-priming of $CD8^+$ CTLs (16, 19, 22, 41, 46-49), thereby driving anti-tumor immunity. A number of strategies are being assessed to activate STING-mediated innate immune sensing and enhance immune priming. For example, ionizing radiation triggers DNA damage, which in turn activates the STING pathway. Preclinical models show that radiotherapy can prime the TME for a better response to checkpoint immunotherapy (19, 50). This combination has also entered into a clinical trial for HPV^- HNSCC (NCT03635164). Another emerging approach is to inhibit the DNA damage repair pathway. Inhibition of either Ataxia-telangiectasia-mutated (ATM) or ataxia telangiectasia and Rad3-related (ATR) proteins, two essential signaling components of the DNA damage response pathway, can induce IFN-I signaling and prime tumors for checkpoint blockade (51, 52). Co-targeting immunosuppressive pathways, such as Il10 signaling, can also improve IFN-I-mediated anti-tumor activity (41). However, as we show in this study, HPV16 E7 functions as a rheostat for IFN-I signaling, which likely limits the cancer cell-specific response to

the aforementioned neoadjuvant therapies. Thus, identification of novel checkpoints of the STING-IFN-I axis informs rational design of immune-priming combinations.

Here we show that NLRX1 is a pivotal intermediary partner that links HPV16 E7 to the suppression of IFN-I. Although the NLR family was initially thought to represent a cytoplasmic counterpart of the TLR family detecting intracellular microbes, accumulating evidence suggests that NLRs fundamentally control the homeostasis of inflammatory signaling and metabolism in addition to sensing microbial threats (53). We first characterized the role of NLRX1 in promoting autophagy in response to RNA virus infection (33). This autophagy-promoting function was later found to be also a central mechanism regulating bacteria- and fungi- host interactions (54, 55). Now we show that the NLRX1-centered autophagy-promoting molecular complex keeps dsDNA viruses-induced immune activation in-check by increasing the turnover of autophagosome cargos that include STING. The production of IFN-I and its downstream target chemokines de novo is a metabolically demanding process. Thus, autophagy recycles excessive proteins, damaged organelles to maintain nutrient supply, and at the same time, increases the turnover of innate immune signaling complexes to keep the cytokines production under control. Together with our previous findings, NLRX1 broadly controls cytoplasmic PRRs-, such as STING- and MAVS-mediated IFN-I production (30, 33, 56), which is hijacked by HPV16 to suppress TIL infiltration. Indeed, NLRX1-deficiency results in many spontaneous rejections of tumors even

using the highly aggressive MOC2-derived tumor models. Depletion of NLRX1 in the tumor cells significantly reduces the exhausted T-cell populations in an IFN-I-dependent fashion. The levels of NLRX1 also correlate with T-cell exclusion among clinical HPV16^{+} HNSCC specimens (Figure 10).

Overall, this study delineates a novel dsDNA virus strategy by which HPV16 E7 functions as a powerful “degrader” of a central innate immune sensing signaling adaptor STING. Our study identifies the NLRX1-mediated autophagic machinery as a potential intervention point to restore the immunogenicity of HPV16^{+} HNSCC. These findings represent a conceptual advance by complementing the current neoantigen-centered framework of cancer immunogenicity.

Methods:

Clinical Samples and Tissue Microarray

The University of Michigan Head and Neck Cancer SPORE recruited patients with previously untreated HNSCC from 2008 to 2012 for a longitudinal study. The patient demographic information is summarized in Supplemental Table 1. The tumors from 297 patients, with a median follow-up of 60.1 months, were incorporated into a tissue microarray (TMA). For each tumor, three representative 5 μm cores, identified by a head and neck pathologist Dr. Jonathan McHugh, were included and stained with anti-STING antibody (LifeSpan BioSciences; LS-B9374). The secondary antibody utilized was biotinylated goat anti-rabbit antibody (Vectastain ABC HRP Kit, PK-4001, Vector Laboratories). Immunohistochemical (IHC) staining density was quantitated using Aperio ImageScope and averaged from the 3 cores. Missing cores and those with insufficient tumor parenchyma were excluded from analysis, and STING IHC scores were available for 264 patients.

Animals

8-week-old C57BL/6 (Strain #000664), *Ifnar1*$^{-/-}$ (Strain #32045-JAX), and *Rag1*$^{-/-}$ (Strain #002216) mice were purchased from Jackson Laboratory (Bar Harbor, ME) and housed under specific-pathogen-free conditions in a temperature and light-controlled environment. As sex is

not a known prognosticator for HNSCC, both sexes were used. Syngeneic HNSCC models were established by inoculating one million empty vector control or shNLRX1 MOC2-E6/E7 cells subcutaneously on the right flank. Beginning on day 7 following tumor implantation, tumors were measured utilizing a digital Vernier caliper every 2-3 days, and tumor volume was calculated according to the formula: ½(length × width^2). All mice were euthanized at the indicated time points. Following euthanasia, the tumors, TILs, lymph nodes, and spleens of the mice were harvested for subsequent analysis.

Cell culture

PCI-13 and SCC90 HNSCC lines were acquired from the University of Pittsburgh. UMSCC47 and UMSCC49 were obtained from the University of Michigan. 93VU147T was provided by Dr. Renske Steenbergen at VU University Medical Center of Amsterdam (57). FaDu was purchased from ATCC (HTB-43). All cell lines were authenticated and maintained in Dulbecco's Modified Eagle Medium (DMEM; 10-013-CV, Corning, Manassas, VA) supplemented with 10% fetal bovine serum (FBS; Gibco, Life Technologies, Carlsbad, CA), 100 U/ml penicillin (Gibco), and 100 mg/ml streptomycin (Gibco). The MOC2-E6/E7 cell line was cultured in 60% Iscove's Modified Dulbecco's Medium (SH30228.01, HyClone, Logan, UT) with 30% F12 nutrient mix (11764-054, Gibco), 5% FBS, 4 µg/ml puromycin, 5 µg/ml insulin, 40 ng/ml hydrocortisone, 5

ng/ml EGF, 100U/ml penicillin and 100 mg/ml streptomycin. All cells were maintained in a humidified incubator at 37°C with 5% CO_2.

Plasmids, Antibodies, Inhibitors, and Antibiotics

The pcDNA 3.1-human STING-HA and pcDNA 3.1-murine STING-HA expression plasmids were provided by Dr. Glen N. Barber at the University of Miami. The CMV-HPV16 E7 (#13686), pEGFP-LC3 (#24920), and lentiCRISPRv2 plasmid (#98290) were acquired from Addgene (Cat. 13686, 24920 and 98290). The short guide RNA (sgRNA) targeting HPV16 E7 sequence is: 5'-CACCGGCAAGTGTGACTCTACGCTT. The pcDNA3.1 empty vector (EV) was described previously (33). Poly(dA:dT) (tlrl-patn-1) and cGAMP (tlrl-nacga23-1) were purchased from InvivoGen (San Diego, CA). Human pGIPZ-shNLRX1-puro and pGIPZ-empty vector-puro lentiviral construct glycerol stocks were obtained from Thermo Fisher Scientific (#NC0744603 and NC9619315, respectively). Mouse pLKO.1-shNLRX1-puro and pLKO.1-empty vector-puro lentiviral constructs were obtained from Sigma Aldrich (Cat. SHCLND-NM_178420and SHC001V). MSCV-C HPV18 E7 retroviral construct (Cat. 37886) and its corresponding control empty vector (Cat.24828) were obtained from Addgene. Lentiviral and retroviral packaging vectors including psPAX2, pMLV gag-pol, and VSV-G were provided by Dr. Jenny P.-Y. Ting at the University of North Carolina at Chapel Hill.

Primary antibodies used for immunoblotting, immunoprecipitation, and immunofluorescence are listed as follows: β-actin (ab49900, Abcam, Cambridge, MA), HPV16 E7 (sc-65711, Santa Cruz Biotechnology, Santa Cruz, CA), HPV18 E7 (sc-365035, Santa Cruz Biotechnology), normal mouse IgG2a (sc-3878, Santa Cruz Biotechnology), NLRX1 for immunoblotting (04-146, Millipore Sigma, Burlington, MA), NLRX1 for immunofluorescence (ab105412, Abcam, Cambridge, MA), phospho-p65 (Ser536) (3033S, Cell Signaling Technology), p65 (8242S, Cell Signaling Technology), phospho-TBK1 (Ser172) (5483S, Cell Signaling Technology), TBK1 (3504S, Cell Signaling Technology), STING (13647S, Cell Signaling Technology), LC3B (2775S, Cell Signaling Technology), HA-HRP (2999S, Cell Signaling Technology), VDAC(4661S, Cell Signaling Technology), p63 (39692S, Cell Signaling Technology). The secondary antibodies utilized for immunoblotting were goat anti-rabbit IgG HRP (ab97051, Abcam) and goat anti-mouse IgG HRP (ab97023, Abcam). The secondary antibodies for immunofluorescence were donkey anti-mouse IgG antibody (Alexa Fluor 488, 715-545-150, Jackson Immunoresearch, West Grove, PA) and donkey anti-rabbit IgG antibody (Alexa Fluor 647, 711-605-152, Jackson Immunoresearch). Bafilomycin A1 was purchased from Sigma-Aldrich (B1793; Ronkonkoma, NY). Puromycin was purchased from InvivoGen (ant-pr-1).

H.&E. staining, Immunohistochemistry, and Immunofluorescence

After the harvest of 5 EV and 5 shNLRX1 tumors from C57BL/6 mice, tumors were fixed with 4% paraformaldehyde (PFA, 15710, Electron Microscopy Sciences) for 24h before dehydration and paraffin embedding. The 5um tumor sections were deparaffinized at 58°C for 20 minutes and then rehydrated. H.&E. and IHC staining were performed as we described. For immunofluorescence staining, cells seeded in chamber slides were incubated with 200 nM MitoTracker (M36008, Life Technologies) for 45 min prior to fixation. After permeabilization with 0.1% Triton X-100 for 10min, the cells were washed and incubated with primary antibodies against HPV16 E7 and NLRX1 at 1:50 dilution at 4°C overnight. Samples were then incubated with secondary antibodies and counterstained with Hoechst 33342 (Cat.H3570, Life Technologies) at room temperature. Images of cells were visualized and captured by a Nikon A1si confocal microscope.

Lentiviral transduction and stable cell line generation

Lentivirus and retrovirus packaging were performed as we have previously described (33). Stable human or mouse NLRX1 knockdown HNSCC cells (including 93VU147T, UMSCC47, SCC90 and MOC2-E6/E7 cell lines) were generated by lentiviral transduction followed by puromycin selection. The cells transduced with empty vector constructs were used as negative

controls. The selecting concentration of puromycin was determined first by establishing a kill curve by adding various doses of puromycin into the wild-type HNSCC cells and determining the lowest concentration that could kill all live cells. The concentrations utilized were 15μg/ml puromycin for 93VU147T, UMSCC47 and SCC90 cell lines, and 120μg/ml puromycin for MOC2-E6/E7 cells. Immunoblotting was performed to validate the knockdown efficiency. In addition, HPV16 *E7* knockout cells were established by transducing HNSCC cells (93VU147T, UMSCC47) with CRISPR-Cas9 lentivirus, and the cells transduced with empty vector virus were considered as a negative control. The knockout of HPV16 *E7* was validated by immunoblotting. HPV18 E7-expressing UMSCC49 cells were established by an HPV18 E7 expression retrovirus, with empty vector retrovirus-transduced tumor cells as a negative control.

Gene expression qPCR and ELISA

Total RNA was extracted using QIAshredder and the RNeasy Plus Mini Kit (Cat. 79654 and Cat. 74134, respectively; Qiagen, Germantown, MD). RNA concentration was measured utilizing a Nanodrop Spectrophotometer (Thermo Scientific). RNA was reverse transcribed into cDNA using High-Capacity cDNA Reverse Transcription Kit and RNase inhibitor (4368814 and N8080119, Applied Biosystems). The primers were synthesized by Integrated DNA technologies

and most of the sequences have been previously described (14). Other primers are as follows: Isg15 F 5'-TGACTGTGAGAGCAAGCAGC, R 5'-CCCCAGCATCTTCACCTTTA, Isg54 F 5'-TCTGGTCACCTGGGGAAACTATG, R 5'-TTCTCAATCCTGTAGGGGCTGG, *Tnf* F 5'-ATGAGAAGTTCCCAAATGGC, R 5'-CTCCACTTGGTGGTTTGCTA; *Il6* F 5'-CTCTGGGAAATCGTGGAAAT, R 5'-CCAGTTTGGTAGCATCCATC; *Il10* F 5'-TAACTGCACCCACTTCCCAG, R 5'-AGGCTTGGCAACCCAAGTAA; *MX1* F 5'-CAATCAGCCTGCTGACATTG, R 5'-TGTCTCCTGCCTCTGGATG; *STING* F 5'-AGCATTACAACAACCTGCTACG, R 5'- GTTGGGGTCAGCCATACTCAG. IFN-β in the supernatant was quantified using a high-sensitivity ELISA kit (41415, PBL Assay Science, Piscataway, NJ).

Immunoblotting and immunoprecipitation (IP) assays

Whole cells lysates in each well were harvested on ice in RIPA buffer (50mM Tris-HCl pH8.0, 1% Triton X-100, 0.05% SDS, 0.25% DOC, 150mM NaCl and 50mM NaF) supplemented with a protease inhibitor cocktail (11836170001, Roche; Pleasanton, CA) and Halt Phosphatase inhibitor cocktail (78420, Thermo Fisher Scientific). The dilutions for the primary antibodies were as following: β-actin 1:100,000, HPV16 E7 1:200, HPV18 E7 1:200, and 1:1000 for other

antibodies. All antibodies were diluted in 5% skim milk. To assess co-IP between HPV16 E7 and STING, control and HA-STING expression plasmids were transfected into empty vector control and NLRX1-deficient 93VU147T cells. After lysates were harvested on ice in IP buffer (50mM Tris-HCl pH8.0, 150mM NaCl and 0.1% NP40) supplemented with a protease inhibitor cocktail (11836170001, Roche), the samples were rotated at 4°C for 30 minutes and centrifugated at 13,000 g for 15 min at 4°C. One-third of the lysates was retained as input controls, while two-thirds of the lysates were used for IP. Supernatants were incubated with anti-HA beads (26181, Thermo Fisher Scientific) at 4°C overnight, gently washed three times in IP buffer, and subjected to a short spin to obtain immunoprecipitated protein complexes. For endogenous co-IP experiments, protein lysates were incubated with HPV16/HPV18 E7-targeted antibodies or IgG2a isotype control, followed by protein A/G UltraLink resin (53132, Thermo Fisher Scientific) pull-down. The protein complexes were resuspended in 1×LDS sample buffer, boiled at 95°C for 5min and then subjected to immunoblotting. Densitometric analysis was conducted relative to the indicated band (specified in the figure legend) using Image J.

AlamarBlue assay

Tumor cells were seeded at a density of 500 cells/well in 96-well microplates with a flat black bottom (3904, Corning; Corning, NY). Every 24 hours from day 1 to day 6, corresponding wells were supplemented with 10% alamarBlue (DAL1025, Invitrogen) and the plate was subsequently incubated at 37°C for 4 hours. The fluorescence intensity (excitation 560, emission 590nm) of these wells was measured using a Biotek plate reader and Gen5 program (version 2.09), and 5 replicates per group were examined simultaneously.

Flow cytometry

Immune cells from tumors, lymph nodes, spleens, and peripheral blood were purified as we have previously described (14), followed by staining for multi-fluorophore flow cytometric analysis with the following antibodies: anti-CD45 (clone 30-F11, Biolegend, San Diego, CA), anti-CD3 (clone 17A2, BD Biosciences), anti-CD4 (clone RM4-5, Biolegend), anti-CD8 (clone 53-6.7, Biolegend), CD16/32 (93, eBioscience) and CD366 (RMT3-23, Biolegend). Cells were also stained for viability using Fixable Viability Dye (FVD) eFluor 780 (65-0865-14, Thermo Fisher Scientific) or Zombie Aqua (423101, Biolegend) diluted 1:1000 in PBS at 4 °C for 30 minutes. Acquisition and compensation were conducted on Beckman Coulter CyAn ADP. FlowJo V10 software was used for data analysis.

Data availability

HNSCC TCGA data are available through http://firebrowse.org/. TCGA raw data are stored in the database of Genotypes and Phenotypes (dbGaP) with the accession number “phs000178”.

Statistics

Statistical analysis between two independent groups was made using unpaired, two-tailed student’s *t*-tests. Comparisons between more than two groups were made using two-way ANOVA with Sidak’s multiple-comparison post-hoc analysis. Spearman’s rank-order correlation was performed to identify correlations between immune cells and IFN-I signature genes. Univariate Cox linear regression modeling was utilized to identify the association between STING expression in TMAs and patient age. The association between STING expression scores and patient survival was conducted using a multivariate Cox regression models. Statistical significance in survival probability between $STING^{low}$ and $STING^{high}$ TMAs was evaluated by Kaplan-Meier survival curves and a log-rank test. Tumor burden between groups was compared using the generalized estimating equation model as we have previously described (14). Statistical significance is indicated in all figures according to the following scale:

*, $p < 0.05$; **, $p < 0.01$; ***, $p < 0.001$; and ****, $p < 0.0001$. All graphs are presented as the mean ± standard error of the mean (SEM).

Study Approval

All animal procedures were performed in accordance with the protocol approved by the Institutional Animal Care & Use Committee at the University of Michigan (PRO00008517). The clinical protocol to obtain HNSCC specimens was approved by the University of Michigan Institutional Review Board (HUM00042189 and HUM00113038), with informed consent obtained from all patients.

Author Contributions:

X. Luo conducted experiments, acquired and analyzed data, and wrote the manuscript. C.R.D. acquired and analyzed data and wrote the manuscript. T.M., B.R.H., L.A.D., Y. H., Y.S.T., W.G., X. Lin and Y.X. conducted experiments, acquired and analyzed data, and reviewed the manuscript. E.B. and B.A.K. analyzed data and reviewed the manuscript. M.A.M., R.L.F., C.B., T.E.C., L.C., M.E.P., S.Y., H.W., P.J.P., G.T.W. and Q.C. provided critical reagents and contributed to the experimental design. Y.L.L. reviewed the data, wrote the manuscript, and was responsible for the overall direction of the project.

Acknowledgments:

This work is supported by NIH grants R01 DE026728, R00 DE024173, R03 DE027399, U01 DE029255, F31 DE028740, T32 AI007413, Rogel Cancer Center research committee grant, National Natural Science Foundation of China grants 81520108009, 81621062, 81730030 and the 111 MOE project of China. We would like to thank the many investigators in the University of Michigan Head and Neck SPORE for their contributions to patient enrollment, tissue procurement and TMA generation. We also thank the patients and their families who tirelessly participated in the study.

References:

1. Secombes CJ, and Zou J. Evolution of Interferons and Interferon Receptors. *Front Immunol.* 2017;8:209.
2. Doehle BP, Chang K, Rustagi A, McNevin J, McElrath MJ, and Gale M, Jr. Vpu mediates depletion of interferon regulatory factor 3 during HIV infection by a lysosome-dependent mechanism. *J Virol.* 2012;86(16):8367-74.
3. Unterholzner L, Sumner RP, Baran M, Ren H, Mansur DS, Bourke NM, Randow F, Smith GL, and Bowie AG. Vaccinia virus protein C6 is a virulence factor that binds TBK-1 adaptor proteins and inhibits activation of IRF3 and IRF7. *PLoS Pathog.* 2011;7(9):e1002247.
4. Ma Z, Ni G, and Damania B. Innate Sensing of DNA Virus Genomes. *Annu Rev Virol.* 2018;5(1):341-62.
5. Gillison ML, Chaturvedi AK, Anderson WF, and Fakhry C. Epidemiology of Human Papillomavirus-Positive Head and Neck Squamous Cell Carcinoma.*J Clin Oncol*. 2015;33(29):3235-42.
6. Saloura V, Fatima A, Zewde M, Kiyotani K, Brisson R, Park JH, Ikeda Y, Vougiouklakis T, Bao R, Khattri A, et al. Characterization of the T-Cell Receptor Repertoire and Immune Microenvironment in Patients with Locoregionally Advanced Squamous Cell Carcinoma of the Head and Neck. *Clin Cancer Res.* 2017;23(16):4897-907.
7. Ferris RL, Blumenschein G, Jr., Fayette J, Guigay J, Colevas AD, Licitra L, Harrington KJ, Kasper S, Vokes EE, Even C, et al. Nivolumab vs investigator's choice in recurrent or metastatic squamous cell carcinoma of the head and neck: 2-year long-term survival update of CheckMate 141 with analyses by tumor PD-L1 expression. *Oral Oncol.* 2018;81:45-51.
8. Ferris RL, Blumenschein G, Jr., Fayette J, Guigay J, Colevas AD, Licitra L, Harrington K, Kasper S, Vokes EE, Even C, et al. Nivolumab for Recurrent Squamous-Cell Carcinoma of the Head and Neck. *N Engl J Med.* 2016;375(19):1856-67.
9. Cohen EEW, Soulieres D, Le Tourneau C, Dinis J, Licitra L, Ahn MJ, Soria A, Machiels JP, Mach N, Mehra R, et al. Pembrolizumab versus methotrexate, docetaxel, or cetuximab for recurrent or metastatic head-and-neck squamous cell carcinoma (KEYNOTE-040): a randomised, open-label, phase 3 study. *Lancet.* 2019;393(10167):156-67.
10. Bauman JE, Cohen E, Ferris RL, Adelstein DJ, Brizel DM, Ridge JA, O'Sullivan B, Burtness BA, Butterfield LH, Carson WE, et al. Immunotherapy of head and neck cancer:

Emerging clinical trials from a National Cancer Institute Head and Neck Cancer Steering Committee Planning Meeting. *Cancer.* 2017;123(7):1259-71.

11. Lau L, Gray EE, Brunette RL, and Stetson DB. DNA tumor virus oncogenes antagonize the cGAS-STING DNA-sensing pathway. *Science.* 2015;350(6260):568-71.
12. Dufour X, Beby-Defaux A, Agius G, and Lacau St Guily J. HPV and head and neck cancer. *Eur Ann Otorhinolaryngol Head Neck Dis.* 2012;129(1):26-31.
13. Alexandrov LB, Nik-Zainal S, Wedge DC, Aparicio SA, Behjati S, Biankin AV, Bignell GR, Bolli N, Borg A, Borresen-Dale AL, et al. Signatures of mutational processes in human cancer. *Nature.* 2013;500(7463):415-21.
14. Tan YS, Sansanaphongpricha K, Xie Y, Donnelly CR, Luo X, Heath BR, Zhao X, Bellile E, Hu H, Chen H, et al. Mitigating SOX2-potentiated Immune Escape of Head and Neck Squamous Cell Carcinoma with a STING-inducing Nanosatellite Vaccine. *Clin Cancer Res.* 2018;24(17):4242-55.
15. Zitvogel L, Galluzzi L, Kepp O, Smyth MJ, and Kroemer G. Type I interferons in anticancer immunity. *Nat Rev Immunol.* 2015;15(7):405-14.
16. Lei Y, Xie Y, Tan YS, Prince ME, Moyer JS, Nor J, and Wolf GT. Telltale tumor infiltrating lymphocytes (TIL) in oral, head & neck cancer. *Oral Oncol.* 2016;61:159-65.
17. Woo SR, Corrales L, and Gajewski TF. Innate immune recognition of cancer.*Annu Rev Immunol.* 2015;33:445-74.
18. Fu J, Kanne DB, Leong M, Glickman LH, McWhirter SM, Lemmens E, Mechette K, Leong JJ, Lauer P, Liu W, et al. STING agonist formulated cancer vaccines can cure established tumors resistant to PD-1 blockade. *Sci Transl Med.* 2015;7(283):283ra52.
19. Deng L, Liang H, Xu M, Yang X, Burnette B, Arina A, Li XD, Mauceri H, Beckett M, Darga T, et al. STING-Dependent Cytosolic DNA Sensing Promotes Radiation-Induced Type I Interferon-Dependent Antitumor Immunity in Immunogenic Tumors. *Immunity.* 2014;41(5):843-52.
20. Deng L, Liang H, Burnette B, Beckett M, Darga T, Weichselbaum RR, and Fu YX. Irradiation and anti-PD-L1 treatment synergistically promote antitumor immunity in mice. *J Clin Invest. 2*014;124(2):687-95.
21. Corrales L, Glickman LH, McWhirter SM, Kanne DB, Sivick KE, Katibah GE, Woo SR, Lemmens E, Banda T, Leong JJ, et al. Direct Activation of STING in the Tumor Microenvironment Leads to Potent and Systemic Tumor Regression and Immunity. *Cell Rep.* 2015;11(7):1018-30.
22. Baird JR, Friedman D, Cottam B, Dubensky TW, Jr., Kanne DB, Bambina S, Bahjat K, Crittenden MR, and Gough MJ. Radiotherapy Combined with Novel STING-Targeting

Oligonucleotides Results in Regression of Established Tumors. *Cancer Res* 2016;76(1):50-61.

23. Moore E, Clavijo PE, Davis R, Cash H, Van Waes C, Kim Y, and Allen C. Established T Cell-Inflamed Tumors Rejected after Adaptive Resistance Was Reversed by Combination STING Activation and PD-1 Pathway Blockade. *Cancer Immunol Res.* 2016;4(12):1061-71.
24. Leach DG, Dharmaraj N, Piotrowski SL, Lopez-Silva TL, Lei YL, Sikora AG, Young S, and Hartgerink JD. STINGel: Controlled release of a cyclic dinucleotide for enhanced cancer immunotherapy. *Biomaterials.* 2018;163:67-75.
25. Hao Y, Yan M, Heath BR, Lei YL, and Xie Y. Fast and robust deconvolution of tumor infiltrating lymphocyte from expression profiles using least trimmed squares. *PLoS Comput Biol.* 2019;15(5):e1006976.
26. Gentles AJ, Newman AM, Liu CL, Bratman SV, Feng W, Kim D, Nair VS, Xu Y, Khuong A, Hoang CD, et al. The prognostic landscape of genes and infiltrating immune cells across human cancers. *Nat Med.* 2015;21(8):938-45.
27. Lei Y, Kansy BA, Li J, Cong L, Liu Y, Trivedi S, Wen H, Ting JP, Ouyang H, and Ferris RL. EGFR-targeted mAb therapy modulates autophagy in head and neck squamous cell carcinoma through NLRX1-TUFM protein complex. *Oncogene.* 2016;35(36):4698-707.
28. Gillison ML. Human papillomavirus-related diseases: oropharynx cancers and potential implications for adolescent HPV vaccination. *J Adolesc Health.* 2008;43(4 Suppl):S52-60.
29. Olthof NC, Huebbers CU, Kolligs J, Henfling M, Ramaekers FC, Cornet I, van Lent-Albrechts JA, Stegmann AP, Silling S, Wieland U, et al. Viral load, gene expression and mapping of viral integration sites in HPV16-associated HNSCC cell lines.*Int J Cancer.* 2015;136(5):E207-18.
30. Guo H, Konig R, Deng M, Riess M, Mo J, Zhang L, Petrucelli A, Yoh SM, Barefoot B, Samo M, et al. NLRX1 Sequesters STING to Negatively Regulate the Interferon Response, Thereby Facilitating the Replication of HIV-1 and DNA Viruses. *Cell host microbe.* 2016;19(4):515-28.
31. Degenhardt K, Mathew R, Beaudoin B, Bray K, Anderson D, Chen G, Mukherjee C, Shi Y, Gelinas C, Fan Y, et al. Autophagy promotes tumor cell survival and restricts necrosis, inflammation, and tumorigenesis. *Cancer cell.* 2006;10(1):51-64.
32. Kimura T, Jain A, Choi SW, Mandell MA, Schroder K, Johansen T, and Deretic V. TRIM-mediated precision autophagy targets cytoplasmic regulators of innate immunity. *J Cell Biol.* 2015;210(6):973-89.

33. Lei Y, Wen H, Yu Y, Taxman DJ, Zhang L, Widman DG, Swanson KV, Wen KW, Damania B, Moore CB, et al. The mitochondrial proteins NLRX1 and TUFM form a complex that regulates type I interferon and autophagy. *Immunity.* 2012;36(6):933-46.
34. Jounai N, Takeshita F, Kobiyama K, Sawano A, Miyawaki A, Xin KQ, Ishii KJ, Kawai T, Akira S, Suzuki K, et al. The Atg5 Atg12 conjugate associates with innate antiviral immune responses. *Proc Natl Acad Sci U S A.* 2007;104(35):14050-5.
35. Liu D, Wu H, Wang C, Li Y, Tian H, Siraj S, Sehgal SA, Wang X, Wang J, Shang Y, et al. STING directly activates autophagy to tune the innate immune response. *Cell Death Differ..*2019; 26(9):1735-1749.
36. Liang Q, Seo GJ, Choi YJ, Kwak MJ, Ge J, Rodgers MA, Shi M, Leslie BJ, Hopfner KP, Ha T, et al. Crosstalk between the cGAS DNA sensor and Beclin-1 autophagy protein shapes innate antimicrobial immune responses. *Cell host microbe.* 2014;15(2):228-38.
37. Moore CB, Bergstralh DT, Duncan JA, Lei Y, Morrison TE, Zimmermann AG, Accavitti-Loper MA, Madden VJ, Sun L, Ye Z, et al. NLRX1 is a regulator of mitochondrial antiviral immunity. *Nature.* 2008;451(7178):573-7.
38. Dharmaraj N, Piotrowski SL, Huang C, Newton JM, Golfman LS, Hanoteau A, Koshy ST, Li AW, Pulikkathara MX, Zhang B, et al. Anti-tumor immunity induced by ectopic expression of viral antigens is transient and limited by immune escape. *Oncoimmunology.* 2019;8(4):e1568809.
39. Shah S, Caruso A, Cash H, Waes CV, and Allen CT. Pools of programmed death-ligand within the oral cavity tumor microenvironment: Variable alteration by targeted therapies. *Head neck.* 2016;38(8):1176-86.
40. Ahn J, Ruiz P, and Barber GN. Intrinsic self-DNA triggers inflammatory disease dependent on STING. *J Immunol.* 2014;193(9):4634-42.
41. Baird JR, Bell RB, Troesch V, Friedman D, Bambina S, Kramer G, Blair TC, Medler T, Wu Y, Sun Z, et al. Evaluation of Explant Responses to STING Ligands: Personalized Immunosurgical Therapy for Head and Neck Squamous Cell Carcinoma. *Cancer Res.* 2018;78(21):6308-19.
42. Shayan G, Srivastava R, Li J, Schmitt N, Kane LP, and Ferris RL. Adaptive resistance to anti-PD1 therapy by Tim-3 upregulation is mediated by the PI3K-Akt pathway in head and neck cancer. *Oncoimmunology.* 2017;6(1):e1261779.
43. Iwasaki A, and Medzhitov R. Toll-like receptor control of the adaptive immune responses. *Nat Immunol.* 2004;5(10):987-95.
44. Peters NE, Ferguson BJ, Mazzon M, Fahy AS, Krysztofinska E, Arribas-Bosacoma R, Pearl LH, Ren H, and Smith GL. A mechanism for the inhibition of DNA-PK-mediated DNA sensing by a virus. *PLoS Pathog.* 2013;9(10):e1003649.

45. Wiest T, Schwarz E, Enders C, Flechtenmacher C, and Bosch FX. Involvement of intact HPV16 E6/E7 gene expression in head and neck cancers with unaltered p53 status and perturbed pRb cell cycle control. *Oncogene.* 2002;21(10):1510-7.
46. Baird JR, Feng Z, Xiao HD, Friedman D, Cottam B, Fox BA, Kramer G, Leidner RS, Bell RB, Young KH, et al. STING expression and response to treatment with STING ligands in premalignant and malignant disease. *PloS One.* 2017;12(11):e0187532.
47. Tan YS, Sansanaphongpricha K, Prince MEP, Sun D, Wolf GT, and Lei YL. Engineering Vaccines to Reprogram Immunity against Head and Neck Cancer. *J Dent Res.*2018;97(6):627-34.
48. Woo SR, Corrales L, and Gajewski TF. The STING pathway and the T cell-inflamed tumor microenvironmen*t. Trends Immunol. 2*015;36(4):250-6.
49. Xu MM, Pu Y, Han D, Shi Y, Cao X, Liang H, Chen X, Li XD, Deng L, Chen ZJ, et al. Dendritic Cells but Not Macrophages Sense Tumor Mitochondrial DNA for Cross-priming through Signal Regulatory Protein alpha Signaling. *Immunity.* 2017;47(2):363-73 e5.
50. Woo SR, Fuertes MB, Corrales L, Spranger S, Furdyna MJ, Leung MY, Duggan R, Wang Y, Barber GN, Fitzgerald KA, et al. STING-dependent cytosolic DNA sensing mediates innate immune recognition of immunogenic tumors. *Immunity.* 2014;41(5):830-42.
51. Zhang Q, Green MD, Lang X, Lazarus J, Parsels J, Wei S, Parsels LA, Shi J, Ramnath N, Wahl DR, et al. Inhibition of ATM increases interferon signaling and sensitizes pancreatic cancer to immune checkpoint blockade therapy. *Cancer Res.* 2019;79(15):3940-3951.
52. Vendetti FP, Karukonda P, Clump DA, Teo T, Lalonde R, Nugent K, Ballew M, Kiesel BF, Beumer JH, Sarkar SN, et al. ATR kinase inhibitor AZD6738 potentiates CD8+ T cell-dependent antitumor activity following radiation. *J Clin Invest.* 2018;128(9):3926-40.
53. Lupfer C, and Kanneganti TD. The expanding role of NLRs in antiviral immunity. *Immunol Rev.* 2013;255(1):13-24.
54. Zhang Y, Yao Y, Qiu X, Wang G, Hu Z, Chen S, Wu Z, Yuan N, Gao H, Wang J, et al. Listeria hijacks host mitophagy through a novel mitophagy receptor to evade killing. *Nat Immunol..*2019;20(4):433-46.
55. Huang JH, Liu CY, Wu SY, Chen WY, Chang TH, Kan HW, Hsieh ST, Ting JP, and Wu-Hsieh BA. NLRX1 Facilitates Histoplasma capsulatum-Induced LC3-Associated Phagocytosis for Cytokine Production in Macrophages. *Front Immunol.* 2018;9:2761.
56. Lei Y, Wen H, and Ting JP. The NLR protein, NLRX1, and its partner, TUFM, reduce type I interferon, and enhance autophagy. *Autophagy.* 2013;9(3):432-3.

57. Steenbergen RD, Hermsen MA, Walboomers JM, Joenje H, Arwert F, Meijer CJ, and Snijders PJ. Integrated human papillomavirus type 16 and loss of heterozygosity at 11q22 and 18q21 in an oral carcinoma and its derivative cell line. *Cancer Res.* 1995;55(22):5465-71.

Figures and Figure Legends:

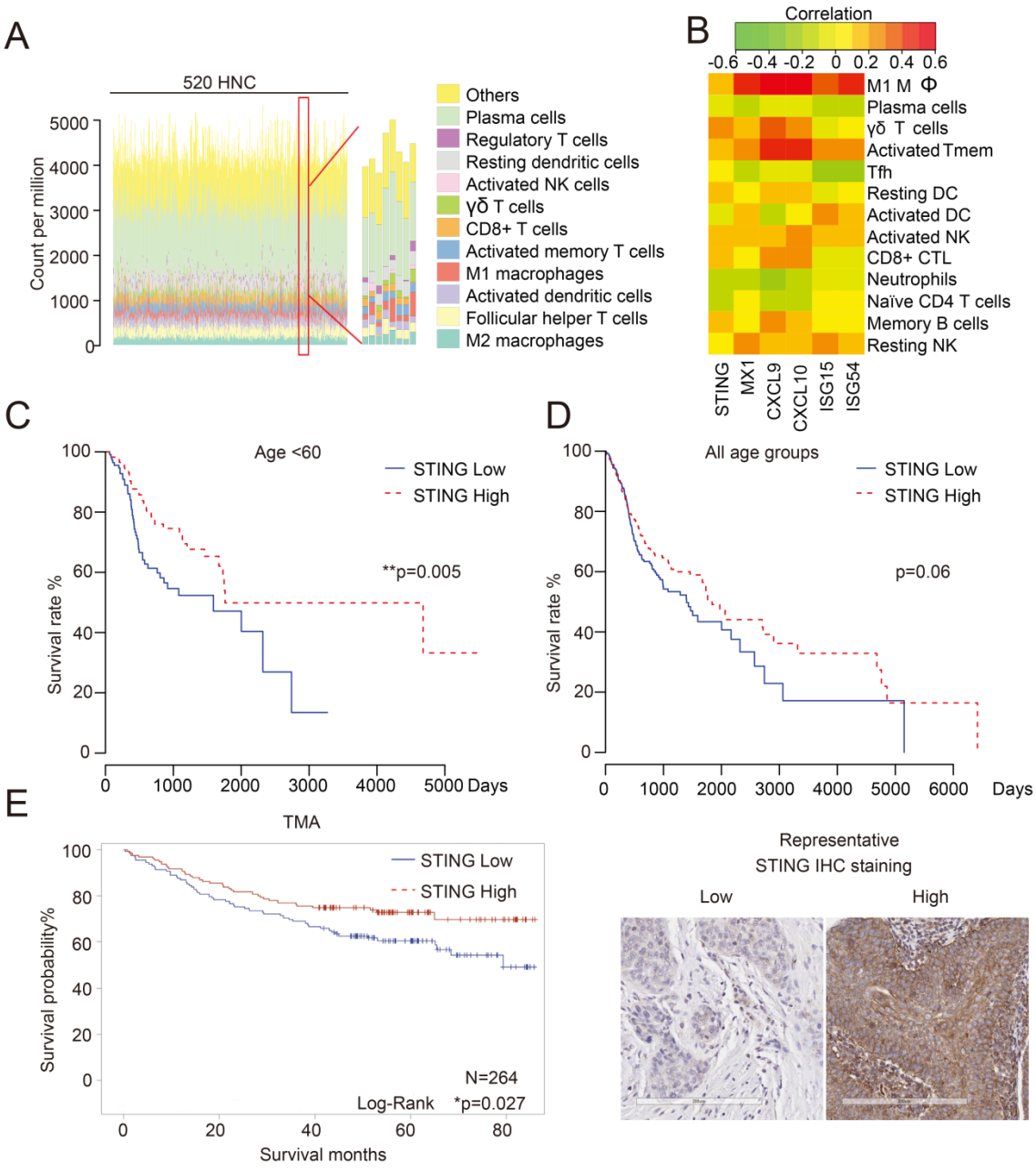

Figure 1. STING correlates with enhanced infiltration of T_H1/Tc1-skewed immune subsets in HNSCC and improved patient survival. (A) Utilizing a machine learning pipeline, we deconvolved tumor-infiltrating lymphocytes (TIL) compositions of 520 human HNSCC

specimens in the TCGA database. Each color represents an immune cell subset, and each vertical line represents one specimen. (B) The correlation between expression levels of type-I interferon (IFN-I) signatures and the percentages of TIL subsets was analyzed by Spearman's rank-order correlation. Positive values indicate positive associations; and negative values indicate inverse associations. (C-D) Kaplan-Meier overall survival analysis was performed based on STING expression in TCGA, presented stratified by age or across all age groups. (E) A tissue microarray (TMA) consisting of 297 HNC with 3 cores for each specimen was stained with STING. Tumor parenchyma and tumor microenvironment (TME) were defined and scored independently using Aperio ImageScope. STING staining scores were available for 264 HNSCC patients. Representative IHC staining for STING are shown on the right panel (scale bar=200μm). Kaplan-Meier survival curves were compared using a log-rank test.

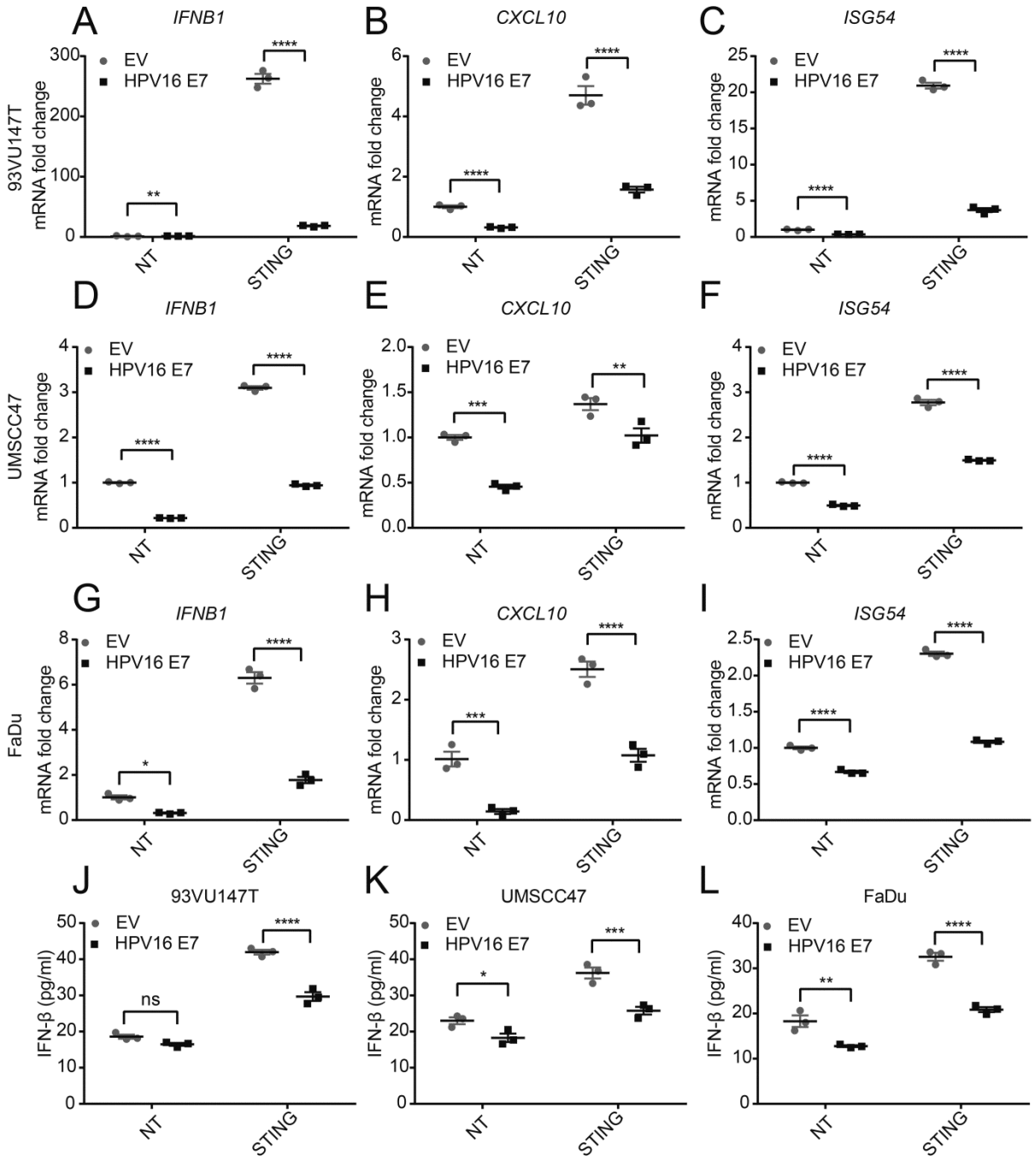

Figure 2. HPV16 E7 inhibits STING-induced transcription of IFN-I target genes in HNSCC cells. (A-C) HPV^{+} 93VU147T, (D-F) HPV^{+} UMSCC47, and (G-I) HPV^{-} FaDu cells were transfected with 1.5 μg/ml STING expression plasmid for 24h with or without transfection of 1.5

µg/ml HPV16 E7 plasmid. The mRNA levels of *IFNB1*, *CXCL10* and *ISG54* were determined by qPCR. Values displayed indicate the mean±standard error of the mean (SEM) of three biologic replicates. The comparisons were made by two-way ANOVA with Sidak's multiple-comparison test. (*p<0.05, **p<0.01, ***p<0.001, and ****p<0.0001). Experiments were repeated twice. 93VU147T (J), UMSCC47 (K), and FaDu (L) cells were transfected with 1.5 µg/ml STING expression plasmid for 24h in the absence or presence of 1.5 µg/ml HPV16 E7 plasmid in three biologic replicate wells. The levels of secreted IFN-β were quantified using ELISA. The comparisons were made by two-way ANOVA followed by a Sidak's post-test (*p<0.05, **p<0.01, ***p<0.001, ****p<0.0001, ns: non-significant). Experiments were repeated twice.

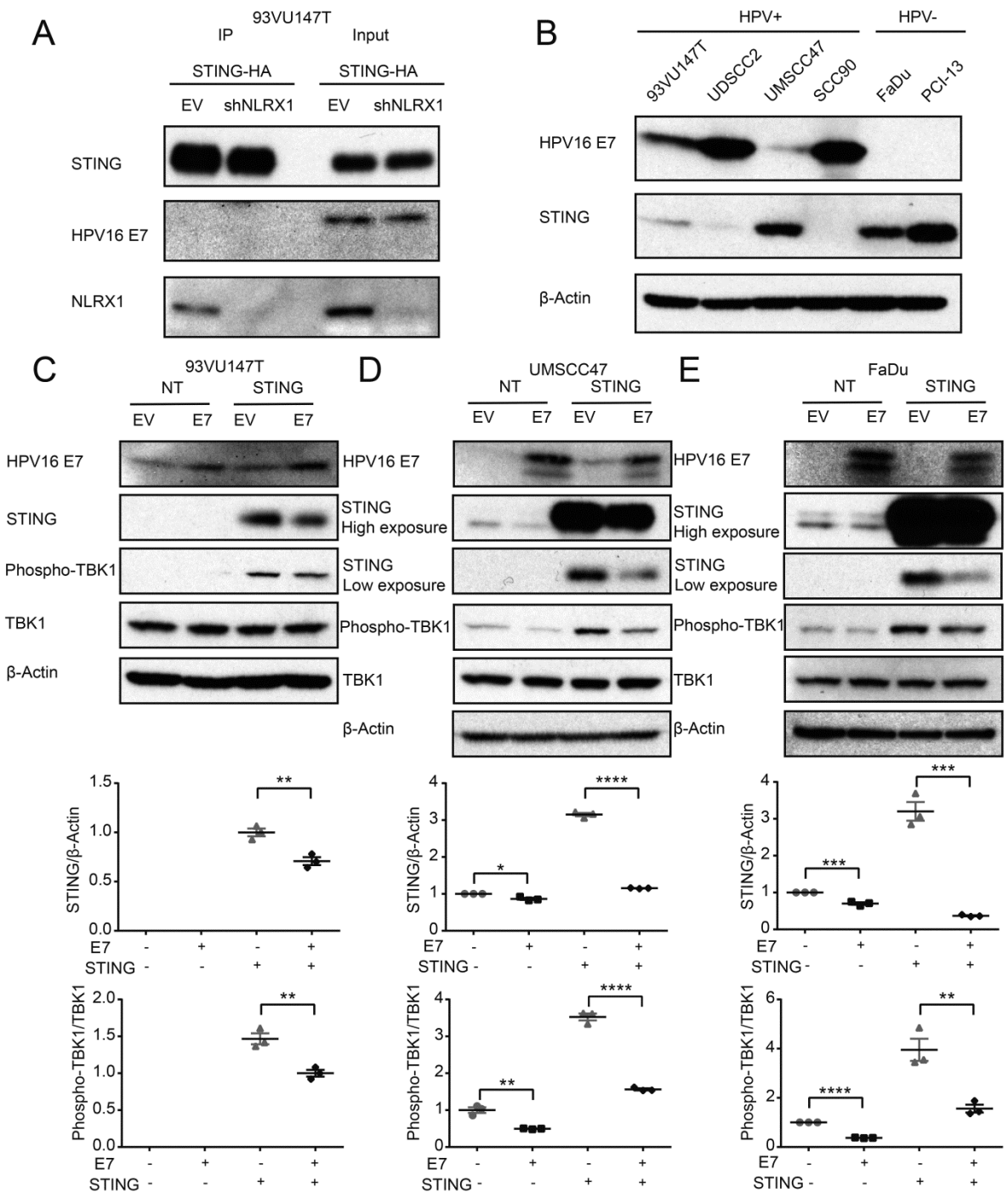

Figure 3. HPV16 E7 attenuates STING-induced innate immune signaling. (A) 93VU147T cells were transduced with empty vector control or sh-NLRX1-expressing lentiviruses to produce stable control and NLRX1-deficient cell lines, which were then transfected with 1.0 μg/ml HA-

tagged STING plasmid and incubated for 16h. STING protein complexes were immunoprecipitated using anti-HA affinity matrix followed by immunoblotting for the indicated potential binding partners. Experiments were repeated for three times, and representative blots are shown. (B) The protein lysates of HPV^+ 93VU147T, UDSCC2, UMSCC47 and SCC90 as well as HPV^- FaDu and PCI-13 cells were harvested on ice and separated by SDS-PAGE. Endogenous expression levels of HPV16 E7 and STING were then detected with respective antibodies. (C-E) 93VU147T, UMSCC47 and FaDu cells were transfected with 1.0 μg/ml STING plasmid and incubated for 24h with or without introduction of 1.5 μg/ml HPV16 E7 plasmid. Cell lysates were immunoblotted with HPV16 E7, STING, and markers for IFN-I activation. Densitometry analysis was performed using ImageJ and shown in the lower panels. Comparison between two groups was made by two-tailed unpaired *t*-test, while comparisons between multiple groups were conducted by one-way ANOVA test followed by Tukey's multiple comparisons test. Results displayed represent the mean±SEM (*$p<0.05$, **$p<0.01$, ***$p<0.001$, and ****$p<0.0001$). Each immunoblot represents 3 biological repeats, and representative blotting results are shown.

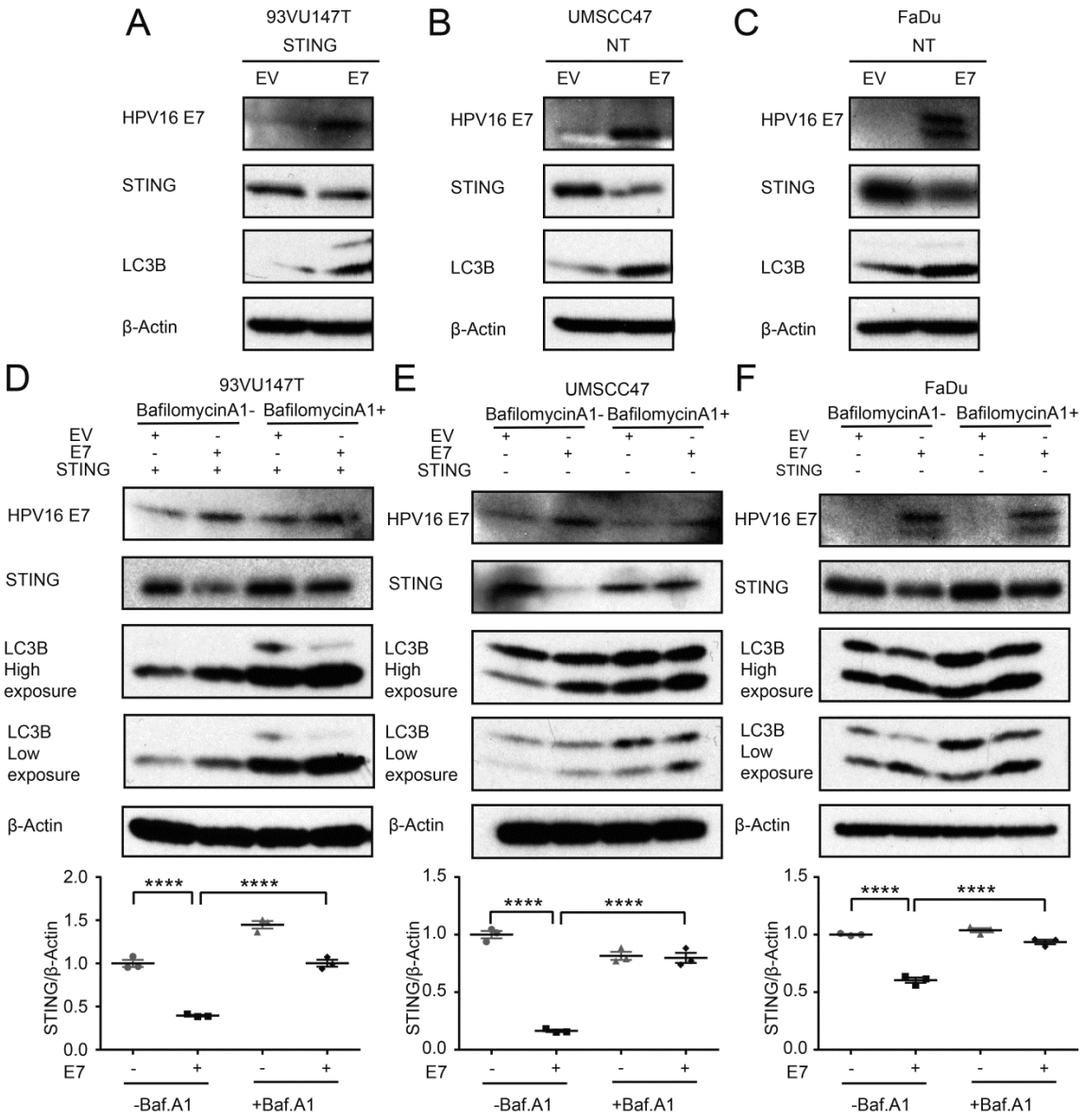

Figure 4. HPV16 E7 promotes autophagy-dependent degradation of STING. (A-C) 93VU147T, UMSCC47 and FaDu cells were transfected with 1.5 μg/ml HPV16 E7 for 24h and 93VU147T alone was simultaneously transfected with STING, and immunoblotting were performed against HPV16 E7, STING and LC3B. Each immunoblot represents 3 biological repeats, and representative blotting results are displayed. (D-F) 93VU147T, UMSCC47 and

FaDu cells were transfected with 1.5 µg/ml HPV16 E7 and incubated for 24h. 93VU147T cells were simultaneously transfected with STING. Half of the groups were then treated with 200nM bafilomycin A1 and incubated for 8h. Cell lysates were immunoblotted for HPV16 E7, STING, and LC3B. Representative blots are shown and represent 3 independent repeats. Densitometric quantitation of STING/β-actin were performed using ImageJ and shown in lower panels. Comparisons between multiple groups were determined by one-way ANOVA test followed by Tukey's multiple comparisons test. Results represent mean ± SEM (****$p<0.0001$).

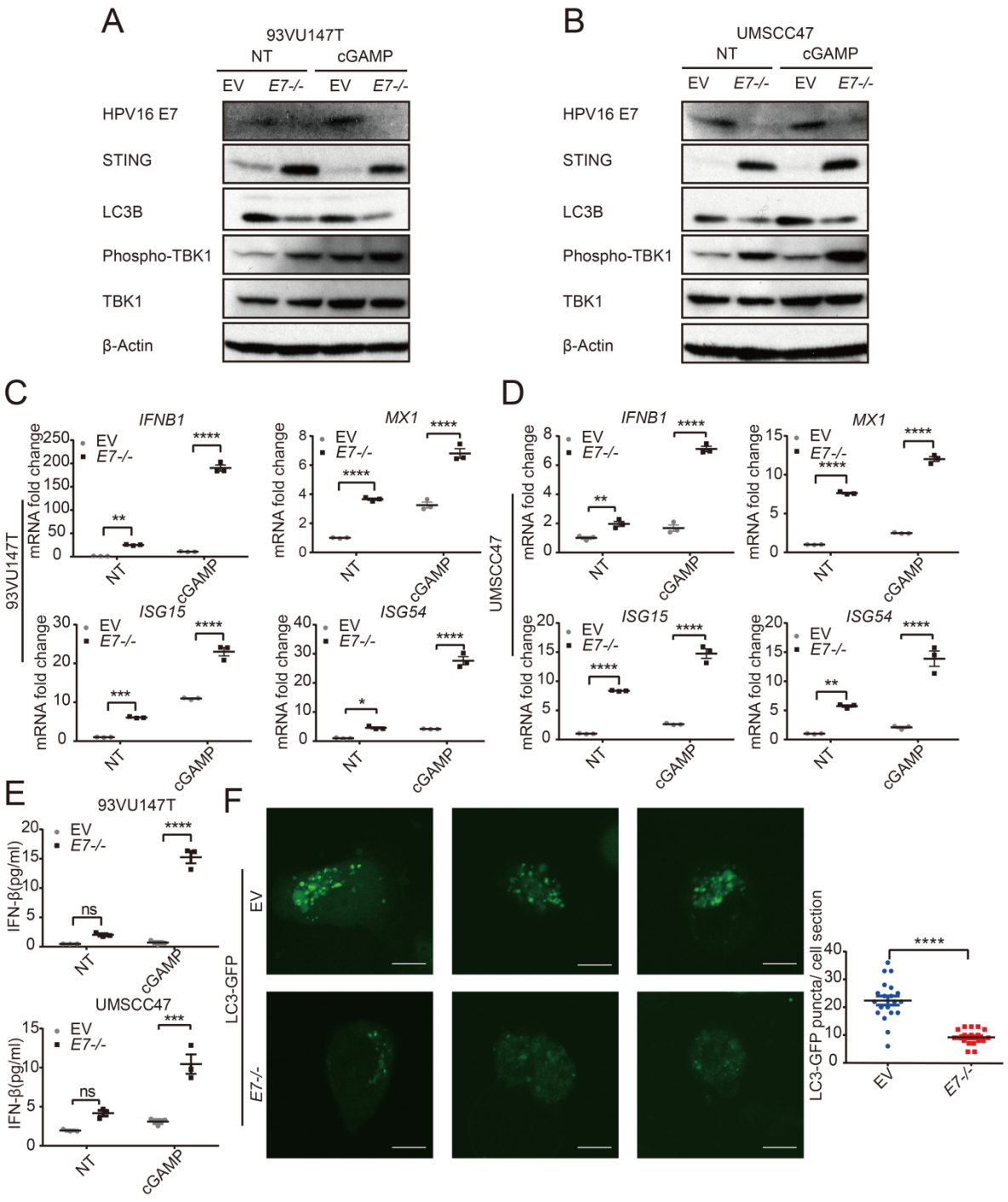

Figure 5. Deletion of HPV16 *E7* restores IFN-I signaling along with reduced autophagic activity. (A-B) 93VU147T and UMSCC47 cells were transduced with lentivirus of CRISPR-Cas9 targeting E7 and the EV was considered as control. The established cell lines were transfected

with STING agonist (cGAMP) or mock for 16h, cell lysates were subjected to immunoblotting for HPV16 E7, STING, LC3B, phospho-TBK1 and TBK1. Representative blots of 2 repeats are presented. (C-D) 93VU147T and UMSCC47 cells with or without the expression of E7 were transfected with cGAMP for 16h and total RNA were isolated. qPCR was then performed to quantitate the mRNA levels of indicated IFN-I signature genes. Values represent mean ± SEM of three biologic replicates. Comparisons were made by two-way ANOVA followed by a Sidak's post-test. (*p<0.05, **p<0.01, ***p<0.001, **** p<0.0001). Experiments were repeated for three times. (E) 93VU147T and UMSCC47 cells with or without the expression of HPV16 E7 were transfected with cGAMP for 16h and the protein levels of IFN-β from supernatant was determined by ELISA. Comparisons were made by two-way ANOVA with Sidak's post-test (***p<0.001, ****p<0.0001, ns: non-significant). Experiments were repeated for two times. (F) Laser confocal analysis was conducted in EV or HPV16 *E7*$^{-/-}$ UMSCC47 cells, which were transfected with pEGFP-LC3 for 48h before capturing the images. Scale bar=10 μm (upper panel). Quantitation of EGFP-LC3 puncta in each cell section of both groups were conducted. Comparisons between the two sets were completed using unpaired two-tailed *t*-test. Values represent mean ± SEM. *n*=20 cell sections from two repeats (lower panel).

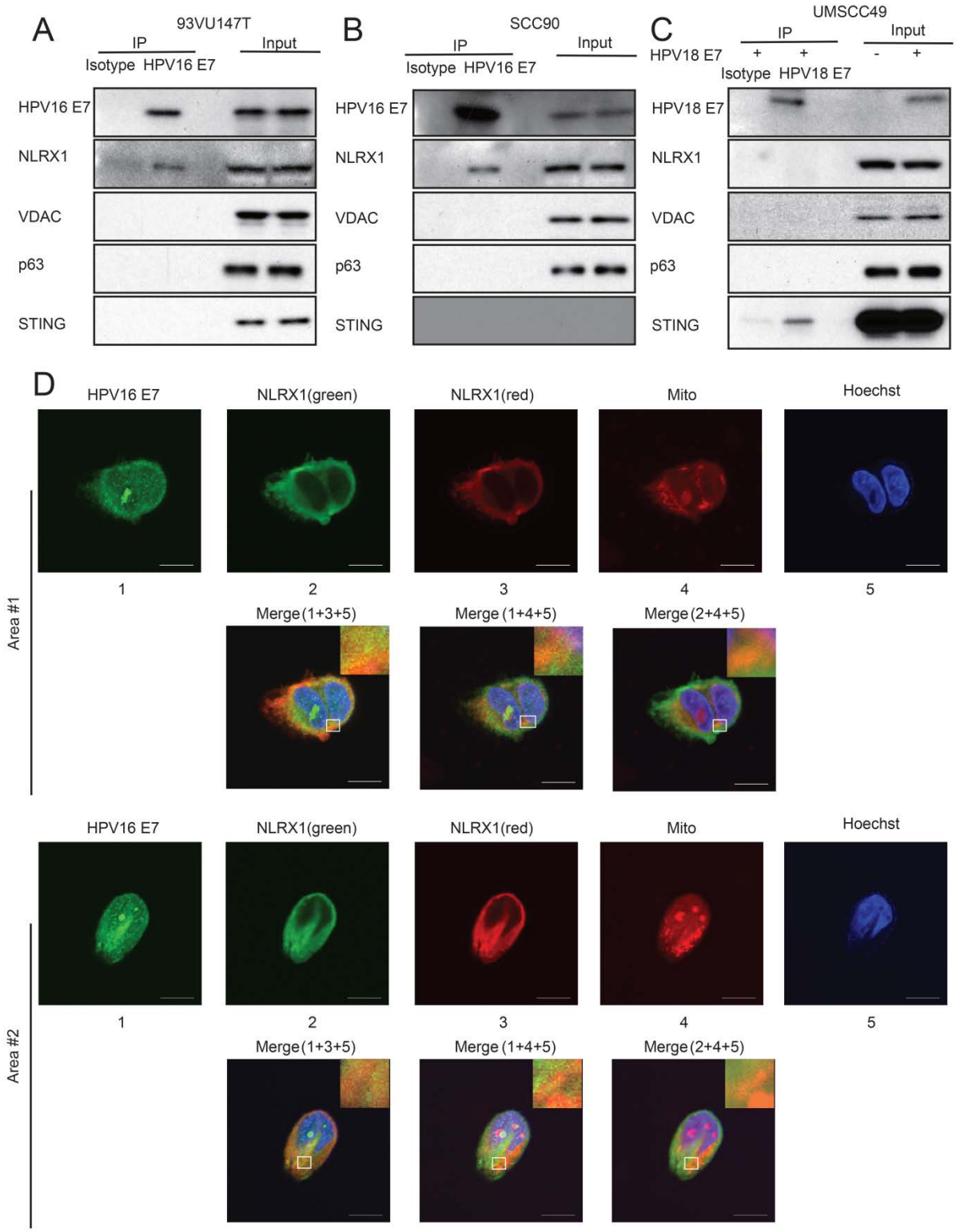
A
93VU147T
IP
Input
Isotype HPV16 E7
HPV16 E7
NLRX1
VDAC
p63
STING
B
SCC90
IP
Input
Isotype HPV16 E7
HPV16 E7
NLRX1
VDAC
p63
STING
C
UMSCC49
IP
Input
HPV18 E7
+ + - +
Isotype HPV18 E7
HPV18 E7
NLRX1
VDAC
p63
STING
D
HPV16 E7
NLRX1(green)
NLRX1(red)
Mito
Hoechst
1
2
3
4
5
Merge (1+3+5)
Merge (1+4+5)
Merge (2+4+5)
Area #1
HPV16 E7
NLRX1(green)
NLRX1(red)
Mito
Hoechst
1
2
3
4
5
Merge (1+3+5)
Merge (1+4+5)
Merge (2+4+5)
Area #2

Figure 6. HPV16 E7 specifically interacts with NLRX1. (A-B) 93VU147T and SCC90 cells were lysed, pre-cleared, and incubated with an isotype control antibody and anti-HPV16 E7. Immunoprecipitation was performed using Protein A/G UltraLink Resin, and immunoprecipitated protein complexes were washed prior to SDS-PAGE. Immunoblotting of NLRX1 and specificity control proteins was carried out. (C)The whole cell lysates of UMSCC49-HPV18 E7-expressing cells were pre-cleared and incubated with IgG2a isotype control or anti-HPV18 E7, followed by incubation with Protein A/G UltraLink Resin for 2h at room temperature. Immunoprecipitated protein complexes were washed and subjected to SDS-PAGE. Immunoblotting of STING and specificity control proteins was performed. Experiments were repeated three times and representative results are shown. (D) 93VU147T cells were stained with MitoTracker, followed by fixation, permeabilization, and staining with NLRX1 and HPV16 E7. Nuclei were counter stained with Hoechst. Representative images and colocalization overlay are shown (scale bar=10 µm). Experiments were repeated twice.

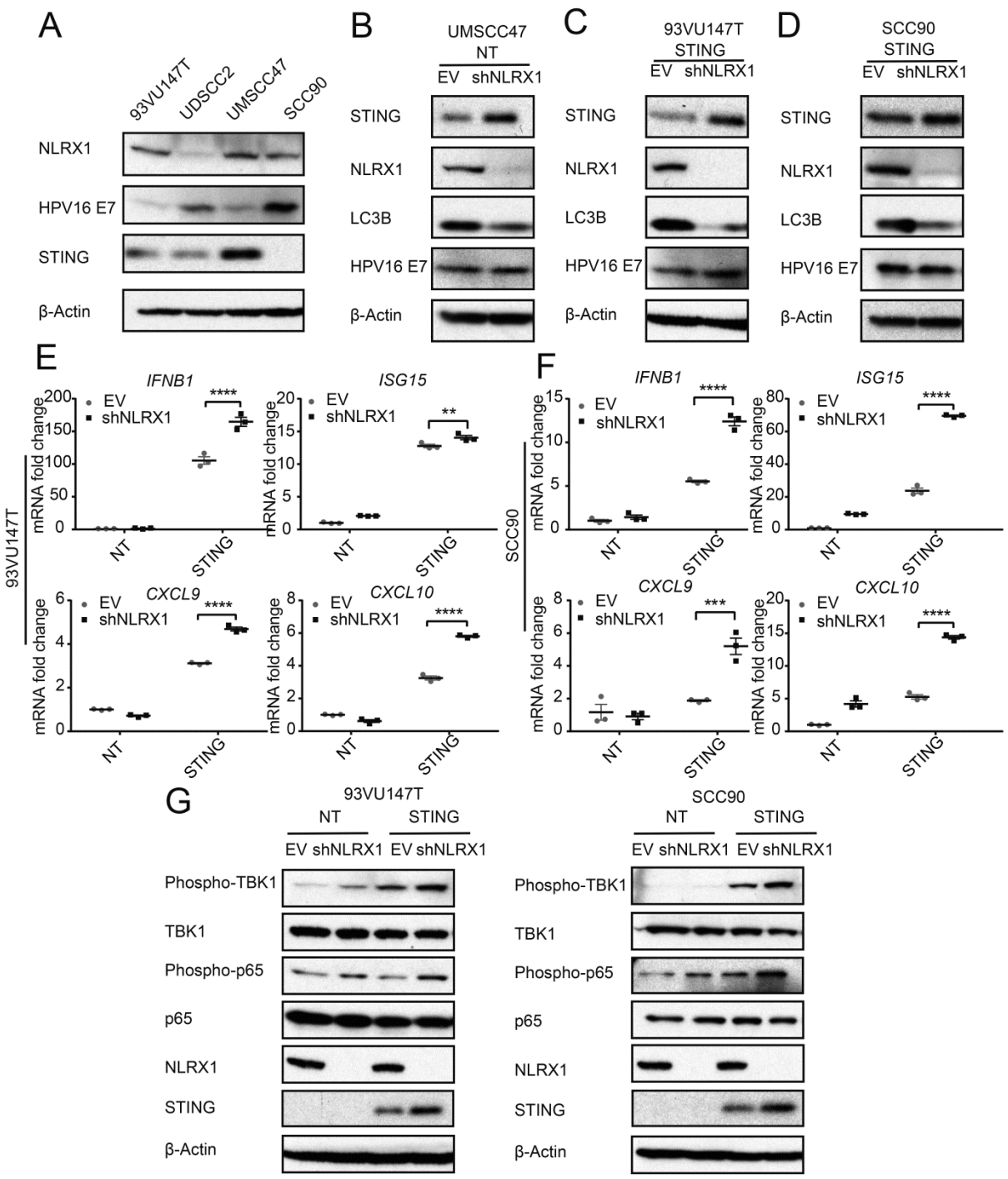

Figure 7. NLRX1 potentiates autophagy-mediated inhibition of STING-IFN-I signaling in HPV16^{+} HNSCC cells. (A) Cell lysates of 4 HPV^{+} HNSCC cell lines were immunoblotted for NLRX1, HPV16 E7, STING, and β-actin. (B-D) UMSCC47, 93VU147T and SCC90 cells were

transduced with lentiviruses carrying an empty vector control construct or an *NLRX1*-targeted shRNA-expressing construct. Stable cell lines were generated through puromycin selection. 1.0 µg/ml empty vector or 1.0 µg/ml STING plasmid was then introduced into 93VU147T and SCC90 cells and incubated for 24h. Cell lysates were separated by SDS-PAGE and immunoblotted for the indicated proteins. Immunoblots were repeated for 2 times, and representative blots are shown. (E-F) Empty vector control or NLRX1-deficient 93VU147T and SCC90 cells were stimulated by 1.0 µg/ml STING for 16h, and qPCR was performed to determine the mRNA levels of *IFNB1, ISG15, CXCL9* and *CXCL10*. Values represent mean ± SEM of three biologic replicates. The comparisons were made by two-way ANOVA with Sidak's multiple-comparison test (**p<0.01, ***p<0.001 and **** p<0.0001). (G) Control and sh-NLRX1 93VU147T and SCC90 cells were transfected with 1.0 µg/ml STING plasmid and incubated for 16h. Cell lysates were then subjected to immunoblotting for markers of IFN-I activation. Immunoblots represent two independent repeats.

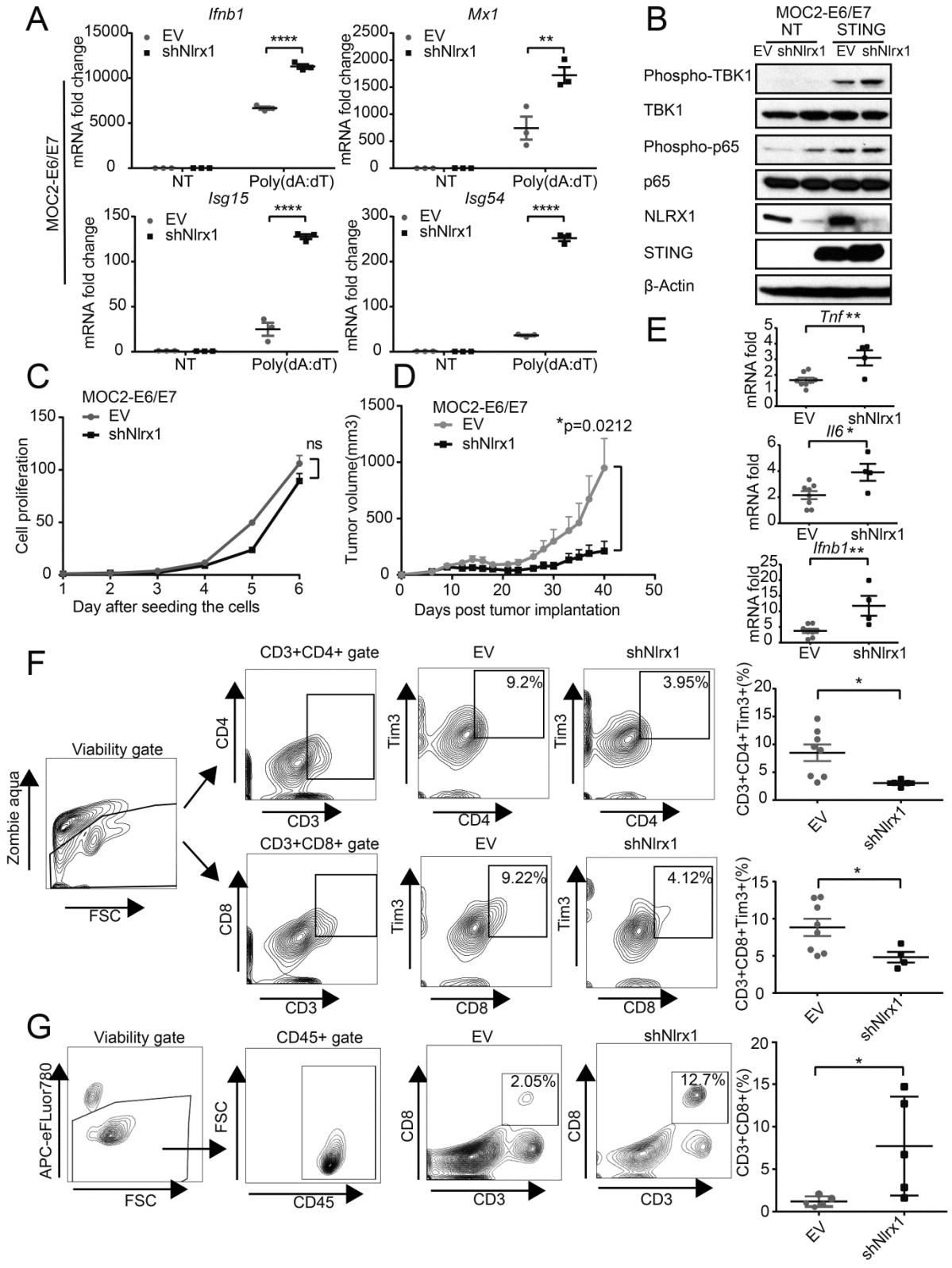
A
Ifnb1
Mx1
Isg15
Isg54
MOC2-E6/E7
mRNA fold change
EV
shNlrx1
NT
Poly(dA:dT)
B
MOC2-E6/E7
NT
STING
EV shNlrx1 EV shNlrx1
Phospho-TBK1
TBK1
Phospho-p65
p65
NLRX1
STING
β-Actin
C
MOC2-E6/E7
Cell proliferation
Day after seeding the cells
ns
D
MOC2-E6/E7
Tumor volume(mm3)
Days post tumor implantation
*p=0.0212
E
Tnf**
Il6*
Ifnb1**
F
CD3+CD4+ gate
CD3+CD8+ gate
Viability gate
Zombie aqua
FSC
CD4
CD8
CD3
Tim3
9.2%
3.95%
9.22%
4.12%
CD3+CD4+Tim3+(%)
CD3+CD8+Tim3+(%)
G
Viability gate
CD45+ gate
APC-eFLuor780
CD45
2.05%
12.7%
CD3+CD8+(%)

Figure 8. NLRX1 in cancer cells inhibits STING signaling in vivo and excludes functional effectors from TME. (A) Control and shNLRX1 MOC2-E6/E7 cells were stimulated by 1.0 μg/ml poly(dA:dT) for 16h and qPCR performed to quantitate the mRNA levels of indicated IFN-I signature genes. Experiments were repeated for three times. Comparisons between two groups were made using a two-tailed unpaired t-test (**p<0.01 and **** p<0.0001). (B) Control and NLRX1-deficient MOC2-E6/E7 cells were transfected with 1.0 μg/ml expression plasmid encoding murine STING and incubated for 16h. Cell lysates were immunoblotted against the indicated markers. Immunoblotting results represent 2 independent repeats. (C) The proliferation of empty vector control and shNLRX1 MOC2-E6/E7 cells was measured by an alamarBlue assay. Each group included five replicate wells. Experiments were repeated twice (ns: non-significant). (D) One million empty vector control or NLRX1-deficient MOC2-E6/E7 cells were implanted subcutaneously at the right flank of C57BL/6 hosts. Tumor measurements were performed every 2-3 days. Tumor burden was compared using the generalized estimating equations model (n=8 in each group;*p<0.05). In vivo experiments were repeated three times with n=19 each group in total. A representative set is shown. (E) Total RNA was isolated from one representative set of tumors and subjected to qPCR. (F) After harvesting tumors, TILs of one representative set were isolated and analyzed by flow cytometry (n=8 in control group, n=4 in shNLRX1 group due to tumor rejection). (G) Lymphocytes were isolated from draining lymph

nodes of one representative set and assessed by flow cytometry (n=5 in each group). Comparisons between two groups from Figure 8 E-G were made using a two-tailed unpaired t-test (*$p<0.05$; **$p<0.01$). Quantifications indicate the mean ± SEM. Results represent three independent experiments.

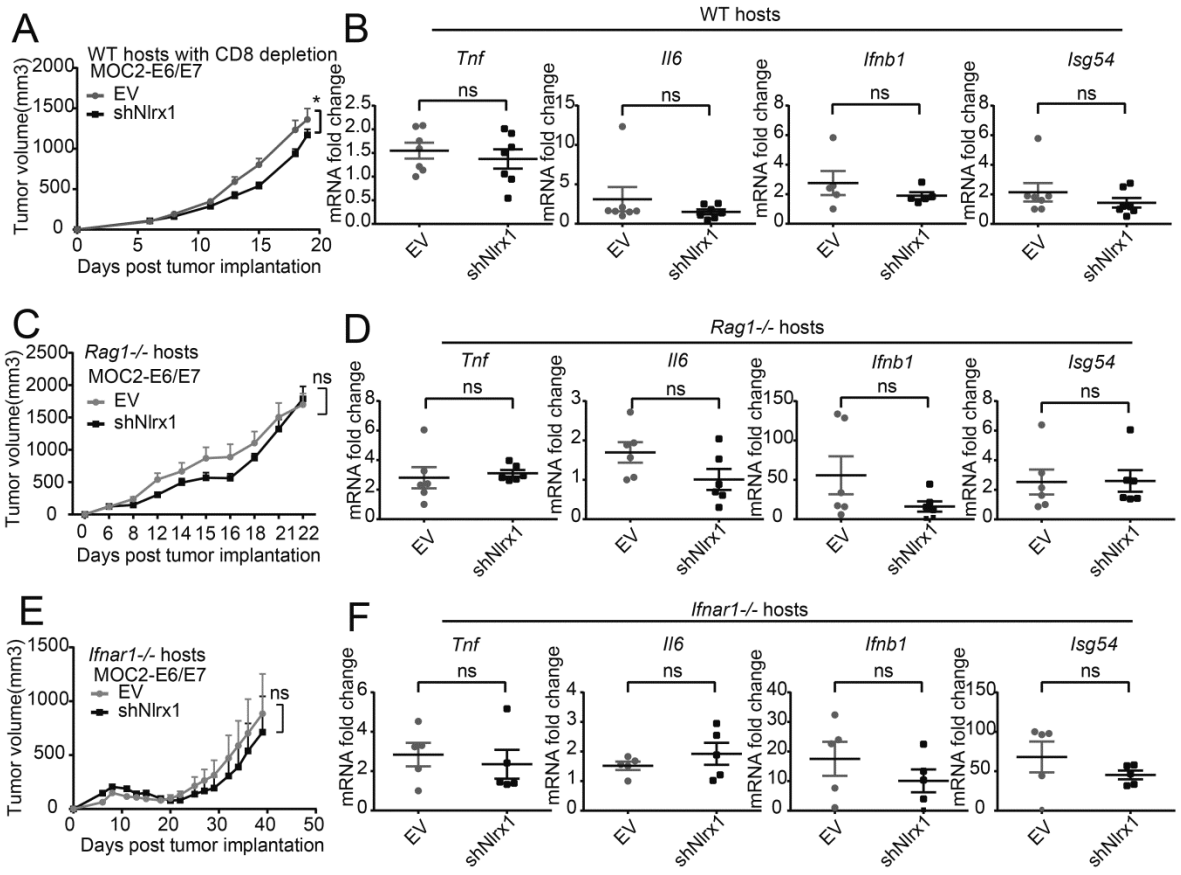

Figure 9. NLRX1-potentiated tumor immune escape is IFN-I-dependent. (A) C57BL/6 hosts were administered with 0.5mg of anti-CD8 or PBS intraperitoneally daily for 3 days before the tumor implantation and then twice per week for two weeks. The overall tumor burden was compared using the generalized estimating equations model (n=7 each group, *p<0.05). (B) Tumors were harvested and total RNA isolated for qPCR detection of the indicated STING signature genes. Values represent mean ± SEM. Comparisons between groups were assessed using an unpaired t-test (ns: non-significant). (C) One million EV control or shNLRX1 MOC2-E6/E7 cells were inoculated subcutaneously at the right flank of *Rag1*$^{-/-}$ mice. Tumors were

monitored and compared as described above (n=6 each group). (D) After euthanization, tumors were harvested and total RNA was isolated. qPCR was conducted to quantify the mRNA levels of indicated genes. Values represent mean ± SEM. Comparisons between groups were assessed using an unpaired t-test. (E) One million EV control or shNLRX1 MOC2-E6/E7 cells were inoculated subcutaneously at the right flank of *Ifnar1*$^{-/-}$ mice (n=5 in control group and n=6 in shNLRX1 group). Tumor growth was monitored and compared as described above. Experiments were performed twice and one representative set is shown. (F) Following euthanasia, all tumors were harvested and total RNA isolated for qPCR analysis. Values represent mean ± SEM. Comparisons between groups were assessed using an unpaired t-test.

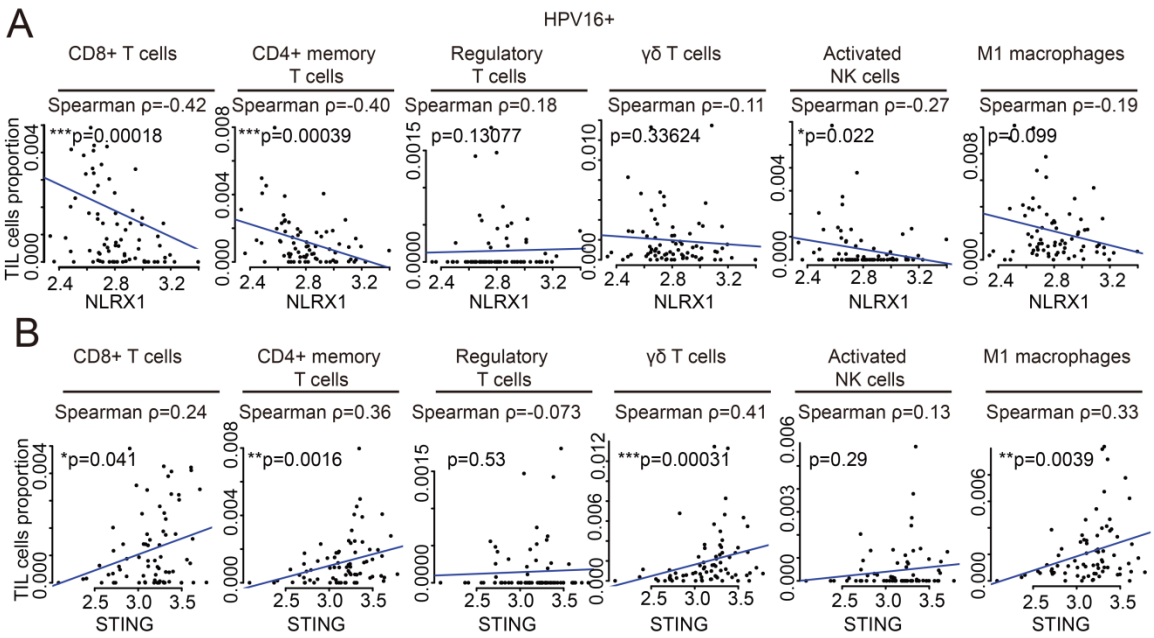

Figure 10. NLRX1 is negatively correlated with anti-tumor immune subsets in HPV$^+$ HNSCC specimens. Spearman correlation analysis was performed to assess the relationship between the expression levels of (A) *NLRX1* or (B) *STING* among 78 HPV16$^+$ HNSCC specimens in the TCGA database and the frequencies of major TIL subsets, with the Spearman correlation coefficients and *p*-values indicated in each panel. Each dot represents one HPV16$^+$ HNSCC specimen. This figure relates to Supplemental Figure 9.

Table 1. The correlation analysis between tumor-specific or Tumor microenvironment (TME)-specific STING staining and patient survival using univariate and multivariate Cox regression models A HNSCC tissue microarray, consisting cores from 297 tumors was stained for STING. Tumor parenchyma and stroma were delineated in Aperio ImageScope. Both tumor-specific and TME-specific scores were recorded. After eliminating cores with insufficient material, scores for 264 tumors were available. A univariate and a multivariate Cox regression model controlling age, stage, site, HPV, and smoking were employed for survival comparisons.

Survival	Univariable Cox		Multivariable Cox	
STING Scores	HR(95%CI)	p-val	HR(95%CI)	p-val
Tumor-Specific	0.99(0.97,0.997)	0.01	0.99(0.98,1.0)	0.049
TME-Specific	0.99(0.97,0.999)	0.04	0.99(0.97,1.0)	0.12